Aus der Klinik und Poliklinik für Nuklearmedizin
der Ludwig-Maximilians-Universität München

Direktor: Prof. Dr. med. Peter Bartenstein

Investigation of models with temporal and spatial interference in image based dosimetry of ^{177}Lu-labelled radioligand therapies

Kumulative Dissertation
zum Erwerb des Doktorgrades der Naturwissenschaften (Dr. rer. nat.) an der
Medizinischen Fakultät der Ludwig-Maximilians-Universität München

vorgelegt von
Dipl.-Phys. Andreas Delker
aus Mainz

2015

Mit Genehmigung der Medizinischen Fakultät der
Ludwig-Maximilians-Universität München

Betreuer: **Priv. Doz. Dr. rer. nat. Guido Böning**

Zweitgutachterin: **Prof. Dr. Kirsten Lauber**

Dekan: **Prof. Dr. med. dent. Reinhard Hickel**

Tag der mündlichen Prüfung: **12.07.2016**

ii

Eidesstattliche Versicherung

Delker, Andreas

Name, Vorname

Ich erkläre hiermit an Eides statt,

dass ich die vorliegende Dissertation mit dem Thema

Investigation of models with temporal and spatial interference in image based dosimetry of 177Lu-labelled radioligand therapies

selbständig verfasst, mich außer der angegebenen keiner weiteren Hilfsmittel bedient und alle Erkenntnisse, die aus dem Schrifttum ganz oder annähernd übernommen sind, als solche kenntlich gemacht und nach ihrer Herkunft unter Bezeichnung der Fundstelle einzeln nachgewiesen habe.

Ich erkläre des Weiteren, dass die hier vorgelegte Dissertation nicht in gleicher oder in ähnlicher Form bei einer anderen Stelle zur Erlangung eines akademischen Grades eingereicht wurde.

München, 16.12.15

Ort, Datum   Unterschrift Doktorandin/Doktorand

List of publications

In this thesis, the following publications are summarized to a cumulative dissertation according to the promotion regulation for natural sciences in the medical faculty of the Ludwig-Maximilians-Universität München:

A. Delker, H. Ilhan, C. Zach, J. Brosch, F-J. Gildehaus, S. Lehner, P. Bartenstein, and G. Böning. "The Influence of Early Measurements Onto the Estimated Kidney Dose in [177Lu][DOTA0, Tyr3] Octreotate Peptide Receptor Radiotherapy of Neuroendocrine Tumors". In: Molecular Imaging and Biology 17 (5 2015), pp. 726-734.

A. Delker, W. P. Fendler, C. Kratochwil, A. Brunegraf, A. Gosewisch, F-J. Gildehaus, S. Tritschler, C. G. Stief, K. Kopka, U. Haberkorn, P. Bartenstein, and G. Böning. "Dosimetry for Lu-177-DKFZ-PSMA-617: a new radiopharmaceutical for the treatment of metastatic prostate cancer". In: European journal of nuclear medicine and molecular imaging 43 (1 2015), pp. 42-51.

Conference abstracts

This work was presented in national and international conferences. The corresponding abstracts were published:

A. Delker, C. Zach, H. Ilhan, P. Bartenstein, M. Hacker, A. Haug, and G. Böning. "The effect of overlying extra-renal uptake on estimated renal doses from planar scans after peptide radionuclide receptor therapy using Lu-177-DOTATATE." In: European journal of nuclear medicine and molecular imaging (Springer). EANM Milan, Italy, 2012.

A. Delker, C. Zach, H. Ilhan, P. Bartenstein, M. Hacker, A. Haug, and G. Böning. "The effect of omitting measurement points in the estimation of renal doses from planar and SPECT scans after peptide radionuclide receptor therapy using Lu-177-DOTATATE." In:

European journal of nuclear medicine and molecular imaging (Springer). EANM Lyon, France, 2013.

A. Delker, C. Zach, H. Ilhan, P. Bartenstein, M. Hacker, A. Haug, and G. Böning. "Überlagerungseffekte bei der Nierendosisbestimmung in planaren Szintigrafien nach der Radiopeptidtherapie mit Lu-177-DOTATATE". In: Nuklearmedizin (Thieme). DGN Hannover, Germany, 2014.

A. Delker, C. Zach, H. Ilhan, P. Bartenstein, M. Hacker, A. Haug, and G. Böning. "Der Effekt ausgelassener Messpunkte bei der Nierendosisbestimmung aus planaren und SPECT Aufnahmen nach der Radiopeptid-Therapie mit Lu-177-DOTATATE". In: Nuklearmedizin (Thieme). DGN Hannover, Germany 2014.

A. Delker, C. Zach, H. Ilhan, J. Brosch, S. Lehner, P. Bartenstein, and G. Böning. "Investigation of the influence of early measurement points onto the kidney dosimetry in Lu-177-DOTATATE PRRT". In: European journal of nuclear medicine and molecular imaging (Springer). EANM Gothenburg, Sweden, 2014.

A. Delker, C. Zach, H. Ilhan, J. Brosch, S. Lehner, P. Bartenstein, and Böning G. "Untersuchung der frühen Nierenkinetik bei der Lu-177-DOTATATE Radiopeptid Therapie". In: Nuklearmedizin (Thieme). DGN Hannover, Germany, 2015.

A. Delker, W. Fendler, A. Brunegraf, A. Gosewisch, F-J. Gildehaus, P. Bartenstein, and G. Böning. "Dosimetry of Lu-177 DKFZ-PSMA-617 for the treatment of metastatic prostate cancer using quantitative SPECT/CT". In: European journal of nuclear medicine and molecular imaging (Springer). EANM, Hamburg, Germany 2015.

A. Delker, W. Fendler, A. Brunegraf, A. Gosewisch, F-J. Gildehaus, P. Bartenstein, and G. Böning. "Dosimetry of Lu-177 DKFZ-PSMA-617 for the treatment of metastatic prostate cancer using quantitative SPECT/CT". In: Journal of Nuclear Medicine 56.supplement 3 (2015), p. 112. SNM Baltimore MD, USA, 2015

Summary

Aim

In targeted radio ligand therapy determination of the regional distribution of the radiation dose is mandatory for the development of therapy strategies which aim for maximizing the therapeutic effect on the tumor, while reducing radiation exposure to healthy tissue. For this purpose, after administration of the therapeutic agent, sequential measurements with a scintillation camera are required to quantitatively assess the kinetics and distribution of the radiopharmaceutical in the body. To improve the accuracy and robustness of existing dosimetric concepts, the kinetic of Lu-177-DOTATATE, a radiopharmaceutical for the treatment of patients with neuroendocrine tumors, was examined in depth. Subsequently, the findings from this study were used to carry out the first image-based dosimetry for the new active substance Lu-177-PSMA, a radiopharmaceutical for the treatment of patients with metastatic prostate cancer. Due to the specific distribution pattern of this ligand, overlay effects in the 2-dimensional (2-D) planar projection were observed. Therefore a quantitative 3-dimensional (3-D) SPECT imaging technique was established and optimized for dosimetry.

Methods

To characterize the dynamics of Lu-177-DOTATATE, whole-body planar projections of 105 patients were recorded at 1, 24, 48 and 72 h after injection. Furthermore, the first hour beginning with the start of the therapeutic agent administration was measured in 12 time frames with duration of 5 min each. An optimal dose model was introduced for the kidneys, for those being a risk organ in this therapy, which consisted of three phases: a linear increase of tracer accumulation during infusion, followed by a 2-phase model being described by a bi-exponential decline. This full data model served as a basis for comparison with reduced data models based on mono-exponentials which made use of all four (at 1, 24, 48 and 72 h after injection) or the last three whole-body scintigraphies.

To support a successful determination of dosimetric values for the new radiopharmaceutical Lu-177-PSMA in a patient study, methods which may overcome the observed activity overlap in planar image projections were evaluated. The most promising approach was to make use of quantitative 3-D SPECT, in which methods to correct for the attenuation of the photon flux, the photon scattering due to electromagnetic interaction and the distance dependent detector blur had to be implemented, followed by the application of a camera-specific calibration factor. The quantitative 3-D SPECT technique was then evaluated for recovery of known activity by a sphere-phantom and subsequently used to reconstruct patient images. Five patients with metastasized prostate cancer received two cycles of Lu-177-PSMA therapy. To characterize and quantify organ and tumor dose distribution caused by this radio therapeutic, patients were imaged with 2-D whole-body scintigraphy and 3-D SPECT/CT at 1, 24, 48 and 72 h after injection. Moreover, blood samples were collected for bone marrow dosimetry in accordance

with the guidelines of the EANM.

Results

The investigation of the temporal distribution pattern of Lu-177-DOTATATE in the kidneys revealed two different pharmacokinetic phases, a fast phase with a mean effective half-life of 25.8 ± 12.0 min and a slow phase with a mean effective half-life of 63.9 ± 17.6 h. By the reduction of the time points to the last four whole-body measurements and the assessment with the reduced data model based on the mono-exponential function, an unacceptable dose underestimation of 12.4 ± 9.2 % compared to the full data model was observed. On the other hand, only a minor deviation from the full data model and thus adequate dose estimation was found by applying the reduced data model to only the latest three days, hence omitting the measurement at 1 h post injection which contained a significant interference by the fast pharmacokinetic phase.

The established quantitative 3-D SPECT technique presented a sufficient recovery of known activity in medium size spherical objects with more than 30 mm diameter (approx. 80 % and above), although a significant underestimation of activity was observed in smaller spheres. With this 3-D dosimetry an estimated dose of 2.2 ± 0.6 Gy for the kidneys (0.6 Gy/GBq), 0.4 ± 0.2 Gy for the liver (0.1 Gy/GBq) and 0.4 ± 0.1 Gy for the spleen (0.1 Gy/GBq) could be reported. The dose to the salivary glands, being assessed with 2-D dosimetry, was 5.1 ± 1.8 Gy (1.4 Gy/GBq). By combining all available 2-D- and 3-D-dosimetric data the absorbed dose of the bone marrow was estimated with 44 ± 19 mGy (0.012 Gy/GBq).

Conclusion

Kinetic analyses of the renal uptake revealed a fast and slow washout phase. Thereby, the slow phase component was found to be responsible to cause the major fraction of the absorbed dose (98.9 %). Although the fast phase did not contribute substantially to the estimated renal dose, it had a high likelihood of interfering with the slow phase within the initial hours after injection. The unexpected dose underestimation which was observed with dosimetry calculations relying on these early time points, such as the reduced data model including the 1h measurement, could finally be explained with this discovery. These underestimations could lead to an over dosage of the therapy activity and thus to a critical radiation exposure to healthy tissue. By omitting this influenced measurement point and the solely use of the last three data points in the reduced data model, the dose delivering phase could be accurately displayed. With the insights gained in this study we were therefore able to develop a dosimetry model and workflow with increased robustness and higher confidence in the reported dose estimates, which at the same time relied on fewer measurements and therefore provided a significant reduction of work load for the staff and overall burden for the patients. This model was then applied in the dose assessment of the new radiopharmaceutical Lu-177-PSMA to avoid the above reported temporal interference effects. Furthermore we observed increased activity accumulations in the intestine after 24 h, which superimposed with the renal activity in the planar image projections and

would thus lead to a falsified determination of activity for this risk organ in 2-D dosimetry. To avoid this spatial interference, the quantitative 3-D SPECT method was established in the clinic and optimized for imaging with Lu-177. The results of the final dosimetry calculations for Lu-177-PSMA indicate a high tumor dose while low dose on healthy tissue was observed. Therefore, an increased therapeutic activity could be recommended in order to maximize the therapeutic effect.

x

Zusammenfassung

Ziel

In der gezielten Radio Liganden Therapie ist die Erhebung dosimetrischer Daten zur Entwicklung angemessener und effektiver Therapieansätze unerlässlich. Ziel ist hierbei, die Strahlendosis für den Tumor und somit den therapeutischen Effekt zu maximieren und gleichzeitig eine möglichst geringe Strahlenbelastung für das gesunde Gewebe zu gewährleisten. Dazu werden nach Gabe des Therapeutikums mehrere Aufnahmen mit einer Szintillationskamera angefertigt, anhand derer die Kinetik und die quantitativ exakte Verteilung des Radiopharmazeutikums im Körper bestimmt werden. In dieser Arbeit wurde zur Verbesserung der bestehenden Dosimetrie Konzepte die Kinetik von Lu-177-DOTATATE, einem Radiopharmazeutikum für die Behandlung von Patienten mit neuroendokrinen Tumoren, eingehend untersucht. Zusätzlich wurden die aus dieser Studie gewonnenen Erkenntnisse verwendet, um die erste bildbasierte Dosimetrie bei dem neuen Wirkstoff Lu-177-PSMA, einem Radiopharmazeutikum zur Behandlung von Patienten mit metastasiertem Prostatakarzinom, durchzuführen. Wegen störenden Bildüberlagerungseffekten bei der bisher verwendeten 2-dimensionalen (2-D) planaren Projektionsmethode wurde des Weiteren eine verbesserte quantitative 3-dimensionale (3-D) SPECT Technik etabliert und für die Dosisbestimmung optimiert.

Methoden

Die Charakterisierung der Dynamik von Lu-177-DOTATATE wurde mittels planaren Ganzkörperprojektionen von 105 Patienten zu den Zeitpunkten 1, 24, 48 und 72 h nach Injektion durchgeführt. Zusätzlich wurde die erste Stunde nach Infusionsstart des Therapeutikums in 12 Zeitfenstern mit einer Dauer von jeweils 5 Minuten gemessen. Für die Nieren, die ein Risikoorgan bei dieser Therapie darstellen, wurde dafür ein optimales 3-Phasen-Dosismodell aufgestellt, das eine lineare Anstiegs-Phase bis zum Maximum der Anreicherung und einen anschließenden 2-phasigen Abfall mittels Bi-exponential-Funktion beinhaltet. Dieses auf allen verfügbaren Daten basierende optimale Modell diente als Grundlage für den Vergleich mit vereinfachten Modellfunktionen, die auf eine reduzierte Datenmenge – die vier (1, 24, 48 und 72h nach Injektion) oder nur die letzten drei Ganzkörperaufnahmen - zur Dosisabschätzung angewendet wurden.

Um eine ausreichend akkurate Dosimetrie des neuen Radio-Therapeutikums Lu-177-PSMA zu ermöglichen wurden vorab Methoden untersucht, die die in planaren Bildprojektionen auftretenden Aktivitätsüberlagerungen kompensieren oder vermeiden. Der vielversprechendste Ansatz war dabei die Verwendung der quantitativen 3-D SPECT Technik, bei der Korrekturmaßnahmen für die Abschwächung der Photonenintensität, für die Streuung der Photonen durch elektromagnetische Wechselwirkung und für die Unschärfe des Detektors in Abhängigkeit vom Abstand implementiert werden mussten. Abschließend wurde für diese Methode ein Kamera-spezifischer Kalibrationsfaktor bestimmt. Die quantitative 3-D SPECT wurde an-

schließend mithilfe eines Kugelphantoms bezüglich ihrer Fähigkeit zur exakten Abbildung bekannter Aktivitätskonzentrationen evaluiert und im Folgenden für die Rekonstruktion der 3-D Patientenbilder angewendet. Bei der Organ- und Tumordosisbestimmung von Lu-177-PSMA wurden bei fünf Patienten, die jeweils zwei Therapiezyklen durchliefen, 2-D Ganzkörperaufnahmen und 3-D SPECT/CT Aufnahmen an den Zeitpunkten 1, 24, 48 und 72 h nach Injektion durchgeführt. Zusätzlich wurden nach den Richtlinien der EANM für die Bestimmungen der Knochenmarksdosen Blutproben der Patienten abgenommen.

Ergebnisse

Bei der Untersuchung des zeitlichen Verlaufs des Radiopharmakons Lu-177-DOTATATE in der Niere konnten zwei unterschiedliche abfallende Phasen beobachtet werden: Eine schnelle Phase mit einer mittleren effektiven Halbwertszeit von 25,8 ± 12,0 min und eine darauf folgende langsame Phase mit 63,9 ± 17,6 h. Bei der Reduktion der Zeitpunkte auf die letzten vier Ganzkörpermessungen und einer Modellierung mit einer mono-exponentiellen Funktion wurde eine inakzeptable mittlere Dosisunterschätzung von 12,4 ± 9,2 % gegenüber dem Referenzmodell festgestellt. Nur eine geringe Abweichung vom Referenzmodell wurde hingegen bei der Verwendung des vereinfachten Modells unter zusätzlichem Auslassen des ersten Messtages und ausschließlichem Fitten an die letzten drei Tage gefunden. Mit diesem Dosimetrie-Modell und Protokoll konnte somit eine robuste und ausreichend genaue Dosisabschätzung gewährleistet werden, und zudem durch die Reduktion der geforderten Messungen eine erhebliche Reduktion des Arbeitsaufwandes für das Personal und der Belastung für den Patienten ermöglicht werden. Die implementierte und optimierte 3-D SPECT Technik erlaubte die Abbildung der Aktivitätskonzentration in mittelgroßen Sphären mit mehr als 30 mm Durchmesser mit einer Genauigkeit von 80 % und mehr, jedoch wurde eine deutliche Unterschätzung kleinerer Objekte beobachtet. Die damit durchgeführte 3-D Dosimetrie zeigte eine Dosisabschätzung von 2,2 ± 0,6 Gy für die Nieren (0,6 Gy/GBq), 0,4 ± 0,2 Gy für die Leber (0,1 Gy/GBq) und 0,4 ± 0,1 Gy für die Milz (0,1 Gy/GBq). Für die Speicheldrüsen wurde eine Dosis von 5,1 ± 1,8 Gy mittels 2-D Dosimetrie ermittelt (1,4 Gy/GBq). Die geschätzte absorbierte Dosis auf das Knochenmark war 44 ± 19 mGy (0,012 Gy/GBq).

Schlussfolgerung

Durch die kinetischen Analysen der Nierendynamik konnten schnelle und langsame Abklingphasen des Radiopharmakons gezeigt werden. Dabei wurde festgestellt, dass der für die Dosis hauptverantwortliche Anteil (98,9 %) von der langsamen Phase ausgeht. Obwohl die schnelle Phase nur einen geringen Anteil an der absorbierten Dosis ausmacht, besteht eine hohe Wahrscheinlichkeit, dass sich diese in den ersten Stunden mit der langsamen Phase überlagert. Die unerwartete Dosisunterschätzung, die in dem reduzierten Datenmodel unter Verwendung der frühen Messung nach einer Stunde auftritt, konnte mit dieser Entdeckung erklärt werden. Diese Unterschätzung könnte bei der weiteren Therapieplanung zu einer Überdosierung der Thera-

pieaktivität und damit zu einer kritischen Strahlenbelastung des gesunden Gewebes führen. Mit Auslassen dieser beeinflussten Messpunkte und der Verwendung der letzten drei Datenpunkte konnte die dosiserzeugende Dynamik hingegen gut abgebildet werden. Mit den Erkenntnissen, die in dieser Studie gewonnen wurden, konnten ein Dosimetrie-Modell und ein Messprotokoll entwickelt werden, mit denen eine fundierte und verlässliche Schätzung der Dosis möglich ist. Gleichzeitig verringern sich aufgrund der reduzierten Messungen der Arbeitsaufwand für das Personal und vor allem die Belastung für die Patienten. Dieses Model wurde dann bei der Dosisbestimmung des neuen Radiopharmazeutikums Lu-177-PSMA angewendet, um die oben genannten zeitlichen Überlagerungseffekte zu vermeiden. Des Weiteren wurde nach 24 h eine vermehrte Aktivitätsanreicherung im Darm festgestellt, die sich in planaren Bildprojektionen mit der Nierenaktivität überlagert und somit zu einer verfälschten Aktivitätsbestimmung für dieses Risikoorgan führen würde. Um diesen Überlagerungseffekt zu vermeiden, wurde die quantitative 3-D SPECT Methode in der Klinik etabliert und für die Bildgebung mit Lu-177 optimiert. Die Ergebnisse der Dosimetrie-Berechnungen für Lu-177-PSMA weisen auf eine hohe Tumordosis bei gleichzeitiger niedriger Dosis auf das gesunde Gewebe hin. Dadurch konnte eine höhere Therapieaktivität empfohlen werden, um den therapeutischen Effekt zu maximieren.

Nomenclature

NET Neuroendocrine tumor

$PRRT$ Peptide receptor radionuclide therapy

2-D 2-dimensional

3-D 3-dimensional

CT Computed tomography

DOTATATE [DOTA^{0}Tyr^3]octreotate

DOTATOC [DOTA^{0}Tyr^3]octreotide

HCT Haematocrit

LOR Line of response

MAPE Mean absolute percentage error

MIRD Medical internal radiation dose

MRI Magnetic resonance imaging

p.i. Post injection

PET Positron emission tomography

PMT Photomultiplier tube

PSF Point spread function

PSMA Prostate specific membrane antigen

PVE Partial-volume effect

RC Recovery coefficient

RM Red marrow

RMBLR Red marrow-to-blood ratio

RMECFF Red marrow extracellular fluid fraction

RoB   Remainder of the body

ROI   Region of interest

SPECT Single photon emission computed tomography

TAC   Time-activity curve

VOI   Volume of interest

Contents

Chapter 1

Introduction

1.1 Targeted radiotherapies

Cancer is still one of the most lethal diseases worldwide. In 2012 14.1 million new cases and 8.2 million deaths were reported [23]. Especially the metastasis of cancerous tumor cells causes an impairment of the health and difficulties in the treatment. In nuclear medicine the targeted radiotherapy is a promising tool for the treatment of patients with metastasized tumors. For this therapy, special characteristics of the tumor cells are utilized, for example the binding of antibodies to prostate specific membrane antigen (PSMA) in the treatment of metastasized prostate cancer [28], or the binding of somatostatin to its receptor on neuroendocrine tumors (NET)[45]. As an example for the treatment of NET, a synthetic somatostatin analogue coupled with a radioactive isotope is injected intravenously to bind to the tumor and irradiate the cancerous cells. The most commonly used compounds for this peptide receptor radionuclide therapy (PRRT) of NETs are octreotide and octreotate which are chemically coupled with the chelate [DOTA^{0}Tyr^3] to DOTATOC and DOTATATE . The DOTA chelator enables the binding with a radioactive isotope to create a tumor specific radiopharmaceutical, the so called tracer. Therefore, it is possible to couple ^{68}Ga, a positron (β^+) emitter, used in the positron emission tomography (PET), to the DOTA chelator for diagnostic examinations or to couple ^{177}Lu, a more aggressive (β^-)-emitting radioactive isotope, to the radiopharmaceutical for the irradiation of the tumor cells [5]. Usually several therapy cycles with intermediate follow-up examinations are performed for the treatment of one patient [37][64]. An example image of a patient's ^{68}Ga-DOTATATE PET image before and after the treatment with ^{177}Lu-DOTATATE with a positive therapy response can be seen in figure 1.1.

^{177}Lu thereby proved to be a convenient isotope for the treatment because of the suitable half-life of 6.6 days for constant irradiation of the tumor over a longer period of time, in contrast to PET tracers whose half-lives are usually in the magnitude of hours. Also the β^- energy with a maximum of 0.5 MeV is favorable. The latter lead to a maximal distance in tissue of approx. 2
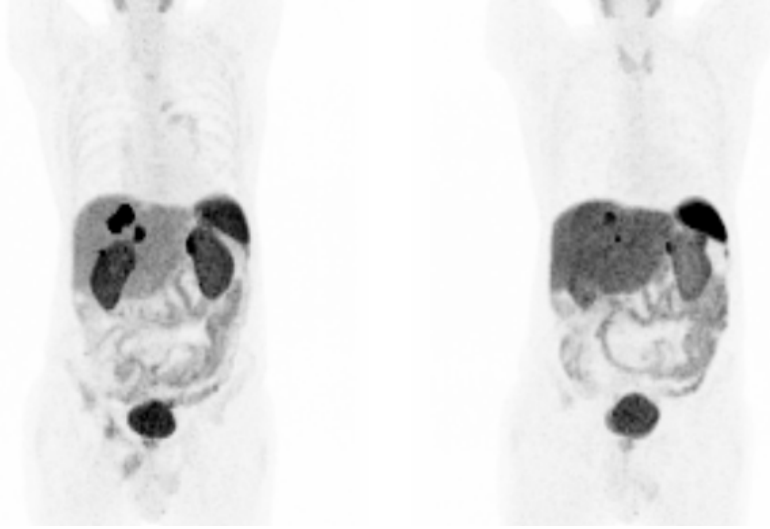
(a) ^{68}Ga-PET image of a NET patient before therapy (b) ^{68}Ga-PET image of a NET patient after therapy

Figure 1.1: PET images of a patient with a hepatic metastatic neuroendocrine tumor of the pancreas, before (left) and after (right) two cycles of ^{177}Lu-DOTATATE therapy

mm which is desirable to target small tumor metastasis and preserve the healthy organs. Another benefit of ^{177}Lu are the additional γ-rays in the decay series with the major peaks at 113 keV and 208 keV [6]. These enable scintigraphic planar images or three dimensional single photon emission computed tomography (SPECT) images within the therapy cycles.

1.2 Dosimetry of radioligand therapies

1.2.1 Organ dosimetry

During the treatment of radioligand therapies not only the cancerous cells but also healthy organs are irradiated by the radioisotope. Therefore dosimetric calculations, especially for the risk organs, have to be performed to spare healthy organs while maximizing the tumor dose. In nuclear medicine, the Committee of Medical Internal Radiation Dose (MIRD) suggested a formalism for the calculation of the absorbed dose (eqn. 1.1)[41]:

$$D_{r_T} = \sum_{r_S} \tilde{A}_{r_S} \cdot S(r_T \leftarrow r_S). \tag{1.1}$$

Due to this formalism the mean dose D [Gy] for a target region r_T is the sum of the dose contributions from all source regions r_S. Thereby the absorbed dose contribution from one source region is calculated by the product of the accumulated activity $\tilde{A}_{r_S}$ [$Bq\cdot$ s] and the source

to target specific S-value $[Gy/(Bq \cdot s)]$. The accumulated activity is the total number of all nuclear disintegrations in one source region over time which is determined by the integral of the time-activity curve (TAC) $A_{r_S}(t)$ (1.2):

$$\tilde{A}_{r_S} = \int_0^\infty A_{r_S}(t)dt. \tag{1.2}$$

In this therapy every patient has different tracer kinetics and the TACs have to be specified individually for all organs and patients. Thereby exponential functions turned out to be feasible TAC-models for the most organs and tumors.

After the determination of all disintegrations in one region, the energy deposition in the regions or volumes of interest (ROI, VOI) is calculated by the S-value. This S-value, sometimes also referred as dose conversion factor, is derived from Monte Carlo simulations of software phantoms for each radionuclide and provides information about the absorbed energy fractions ϕ from a certain source region r_S to a target region r_T with the mass M [kg]. The calculation of the S-values is performed by

$$S(r_T \leftarrow r_S) = \frac{\sum_i E_i \phi_i(r_T \leftarrow r_S, E_i)}{M(r_T)} \tag{1.3}$$

with the energy E [J] transmitted at each disintegration. The S-values for the most common nuclides and major source organs are published in scientific journals [55][22][58], or in the online retrievable RADAR database [59].

Patient individual scaling

A drawback of the MIRD S-value method is that patient individual characteristics are not included. The patient size and the mass of the organs sometimes differ significantly from the Monte Carlo phantoms. To regain more patient individual dose calculations, WILLIAMS et al. suggested correction factors for the dose estimates for internal β^- emitters [62]. Thereby the S-value of the phantom is scaled according to equation 1.4,

$$S(patient) = S(MIRD) \cdot \frac{m(MIRD)}{m(patient)}, \tag{1.4}$$

with the phantom and patient mass to obtain the individual patient S-value. Nevertheless for a more specific dose calculation direct Monte Carlo simulations or dose kernel convolution methods should be considered [31].

1.2.2 Bone marrow dosimetry

The irradiation of the red marrow (RM) is a special case in the dosimetry of radioligand therapies. According to the guidelines of the European association of nuclear medicine (EANM)[33], the RM-dose can be described as the dose fractions from the bone marrow self-dose ($D_{RM \leftarrow RM}$), the cross irradiation of the major source organs ($D_{RM \leftarrow Organs}$) and the remainder of the body

$(D_{RM \leftarrow RoB})$(eqn. 1.5), whereby the last two can be obtained from therapy images:

$$D_{RM} = D_{RM \leftarrow RM} + \sum_{rS} D_{RM \leftarrow Organs} + D_{RM \leftarrow RoB}. \qquad (1.5)$$

The bone marrow self-dose can be assessed by the activity concentration in blood with the method suggested by SGOUROS (eqn. 1.6) [52]:

$$D_{RM \leftarrow RM} = [\tilde{A}]_{blood} \cdot \underbrace{\frac{RMECFF(= 0,19)}{1 - HCT}}_{RMBLR} \cdot m_{RM,phantom} \cdot S_{RM \leftarrow RM,phantom}. \qquad (1.6)$$

For this purpose, blood samples of the patient at different therapy stages have to be collected and the contained activity concentration measured. After obtaining the area under the curve of the activity concentration, the red marrow dose can be calculated by the product of this accumulated activity concentration ($[\tilde{A}]_{blood}$), the mass ($m_{RM,phantom}$), the S-value ($S_{RM \leftarrow RM,phantom}$) and the red marrow-to-blood ratio (RMBLR). The RMBLR is composed of the red marrow extracellular fluid fraction (RMECFF), which is assumed equal 0.19 and the patient's haematocrit (HCT) [52].

1.3   Imaging in nuclear medicine

The main purpose of imaging modalities in nuclear medicine is to investigate functional processes of cells and organs in vivo with the help of concentration distributions of radioactive tracers. The main tomographs in nuclear medicine, the PET and the SPECT, may be coupled to a computed tomography (CT) (PET/CT, SPECT/CT) or recently also to a magnetic resonance imaging (MRI) tomograph (PET/MRI) into a multimodal imaging device to have the advantage of the structural and functional information in one examination [9][10][27][46]. These devices are suitable to determine the time activity curves $A_{rS}(t)$ needed for dosimetry calculations (cf. eqn. 1.2).

1.3.1   Planar gamma camera images

A gamma camera, also called scintillation- or Anger camera, consists of one or more (usually two) detector heads, which are capable to detect γ-photons. Thereby, a γ-ray could interact and excite the detector's crystal, which is usually a sodium-iodine crystal doted with Thallium (NaI(Tl)). As a consequence, during relaxation of the excited crystal, it scintillates in the visible light range. This light signal is then converted and amplified into an electrical signal by a grid of photomultiplier tubes (PMT). A following signal processing electronics allows a spatial information of each incident by performing a center of mass calculation amongst the PMT-signals. Moreover, energy information of the detected photon is obtained by the sum over
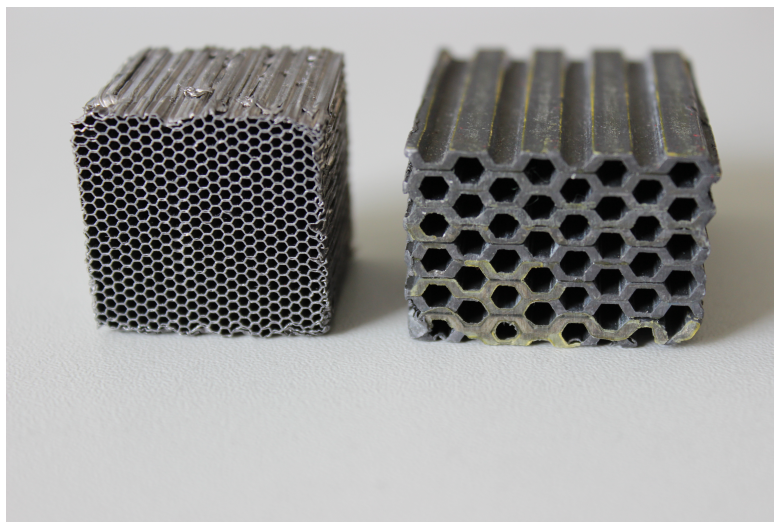
Figure 1.2: Two cropped pieces from a low energy (left) and an high energy collimator (right)

the signals of all PMTs [1].

Only γ-ray photons with a known input direction onto the detector are suitable to assemble an image. Therefore, the impinging photon angle is limited by a collimator in front of the scintillation crystal. A collimator is usually structured with several layers of lead which are joint together to a honey-comb structure with holes for the photons to pass. The diameter and length of the holes determines the possible resolution of the system, whereas the thickness of the septa between the holes and the length of the collimator defines the applicable photon energy. In figure 1.2 two parts of different collimators are presented. The collimators used in this work are exclusively medium energy parallel hole collimators, suitable for the γ energy of ^{177}Lu.

By positioning the detector heads over the desired anatomical region, a planar 2-dimensional (2-D) projection of the activity distribution of the patient can be measured. Alternatively a constant motion of the camera bed can cover a wider region up to whole-body planar images. Thereby the usage of two or more camera heads allows the simultaneous measurement of different angles. Another possibility is the division of one measurement into smaller time frames. Thereby temporal information of the activity accumulation can be obtained.

1.3.2 Single Photon Emission Computed Tomography - SPECT

In principle the SPECT camera consists of the same detectors and collimators as the γ-camera with the addition of a rotatable gantry which enables the motion of the detectors around the patient. An example of a two head SPECT camera is shown in 1.3. In a SPECT measurement the detector rotates in angular steps around the long side of the patient and records multiple projections. These together with computed image reconstructions generate 3-dimensional (3-D)

Figure 1.3: Image of a Siemens Symbia Intevo T16 SPECT/CT during a rotation around the camera table

images of the tracer distribution in the patient [48][53][34].

A major advantage of the γ- or SPECT camera is the variety of different radioactive isotopes which can be measured. Besides isotopes with a γ component, even pure β^- emitters like ^{90}Y can be recorded because of the Bremsstrahlung [2][61]. This enables the radiochemistry to produce versatile tracers for diagnostic purposes and therapy monitoring.

1.3.3   Positron Emission Tomography - PET

The positron emission tomography system is based on a circular detector array with a gantry bore diameter of 70 to 90 cm [60][36][7]. The structure of these detectors, with a crystal and photomultipliers (or semiconductors) is similar to the γ-camera but in contrary does not require collimators to determine the line of response (LOR).

For this imaging modality the proton-rich PET nuclides (X) with the atomic number (A) and the nucleon number (Z) disintegrate by β^+ decay under the emission of an electron neutrino (ν_e) and a positron (e^+) to the new element (Y) by transforming one proton to a neutron (cf. equation 1.7).

$$\ _A^Z X \longrightarrow \ _{A-1}^Z Y + e^+ + \nu_e \tag{1.7}$$

The positron loses its kinetic energy through interaction with matter and combines with an electron situated in the environment after few micro- to millimeters. It annihilates to two equivalent

photons flying in almost opposite directions. Due to the conservation of the positron's momentum a small deviation from 180 degree might occur. Both photons, each with an energy of 511 keV because of the mass-energy equivalence, then arrive nearly simultaneously within a few nanoseconds at opposing detectors. This coincidence event defines the line of response (LOR) from which the tracer distribution can be reconstructed with similar image reconstruction techniques as utilized in SPECT. This electronic collimation does not require physical collimators and therefore leads to higher sensitivity and better resolution compared to SPECT. Furthermore if a PET isotope can be coupled to a therapy compound, this image technology is favorable for pre-therapy examinations and follow-up monitoring.

1.4 Image degrading factors and calibration

In a variety of nuclear medicine image analysis the absolute quantitative concentration needs to be assessed. Especially for dosimetry an exact activity quantification is needed. Therefore correction methods have to be applied to compensate for several image degrading factors, followed by camera calibration. In the following paragraph, the main image errors are introduced qualitatively. For further descriptions of these effects the reference books of BAILEY et al. and ZAIDI et al. are recommended [3][47].

1.4.1 Photon scattering

Due to the Compton effect the γ-photons are scattered in matter and consequently the detector could measure events with a wrongly assumed origin. Thereby the initial wavelength λ changes to λ' after the scattering of the angle Θ (eqn. 1.8), with the constants m_e for the electron rest mass, c for the speed of light and h for the Planck constant.

$$\lambda' - \lambda = \frac{h}{m_e c}(1 - cos\Theta) \tag{1.8}$$

Especially scattered photons from higher γ-ray emissions into the energy acquisition window are problematic. As a consequence, this leads to increased noise and overestimation of counts in the activity determination.

1.4.2 Photon flux attenuation

Another image degrading effect is photon flux attenuation described by the Beer-Lambert law (eqn. 1.9). From an emitted initial intensity I_0 a fraction of the photons is absorbed by the photo effect or scattered outside the LOR. In dependence of the mass attenuation coefficient μ and the distance x in matter, only a reduced intensity $I(x)$ is measured:

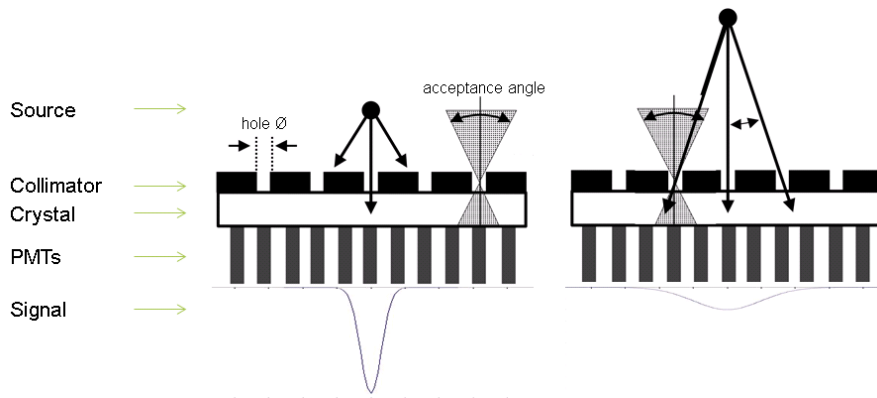$$I(x) = I_0 e^{-\int \mu(x)\, dx}. \tag{1.9}$$

Figure 1.4: Scheme of the distance dependent detector blur. Left: The photons emitted by a point source near the collimator surface only pass through one hole which results in a sharp signal. Right: The photons of a point source further away from the collimator surface are within the acceptance angle of adjacent holes. Consequently the signal of the point source is blurred. The image was provided by courtesy of Dr. Boening

Therefore the measured counts should be upwardly corrected, based on the covered path and the accumulated attenuation coefficient to not underestimate the measured activity.

1.4.3 Distance-dependent image blur in SPECT

In nuclear medicine the resolution of a camera system is the ability to distinguish separated sources of radioactivity. This resolution is dependent of the spatial position of the source. Although all nuclear imaging methods suffer from effects which degrade the spatial resolution, here only the distance-dependent detector blurring in SPECT measurements is illustrated in figure 1.4, because of the higher relevance of SPECT in this work.
The radiation of a point-source near the detector only passes through a few, or in this example one collimator hole onto the scintillation crystal and generates a sharp signal, which could be differentiated from the next source. If the point-source is farther away, the γ-rays are also in the acceptance angle of the aperture of the next collimator holes and the resulting signal is broadened by this effect which impairs the resolution.

1.4.4 Dead time

Besides the already introduced spatial image degradations, also the temporal count rate of the detectors are limited and contribute to a decline of the image quality and absolute number of measured counts. For SPECT cameras this effect appears at high activity concentrations and thus at high count rates approximately over 40 kilo counts per second [63]. After a true radiation event each detector system needs a certain recovery time before the next pulse can be counted. All photons arriving the detector during this dead time aren't processed and are lost for the
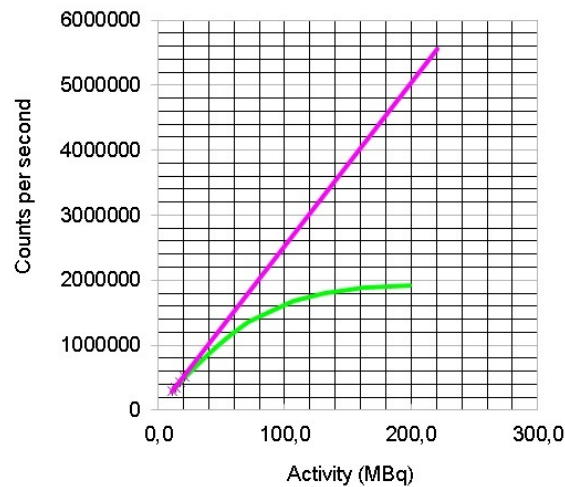
Figure 1.5: Graph of a dead time measured at the Siemens Inveon microPET system. The purple line represents the estimated cps signal for the corresponding activity without dead time, whereas the green curve, plotted from measurement results, depicts the reduced count rate in dependency on the increased activity.

counting statistics.

Figure 1.5, measured with a Siemens Inveon microPET system illustrates this effect. While the estimated real count rate increases linearly (purple), the slope of the count-signal for the true coincidences decreases.

1.4.5 Partial-volume effect and spill-over

These two effects arise by the finite sampling and spatial resolution of the imaging system [56]. Because the sampling of the voxel matrix (3-D image array of volumetric pixels) often insufficiently maps the contours of the tracer distribution, voxels often include different tissue types. Consequently such a voxel contains the fractionated activity signal of all underlying tissues. This partial-volume effect (PVE) blurs and therefore reduces the activity signal at the edges of tracer distributions. The other effect, the spill-over, occurs because of the limited resolution of the system. As a result, the signal of a small source is blurred over a larger area, over the edges of its actual border. Moreover the maximal intensity of the activity signal decreases with the broadening. In case of adjacent source regions the activity signal spills in and out from each region which could also create a distorted activity estimation. Both effects are often grouped together under the term PVE.

1.4.6   Calibration

Before a quantitative image is obtained, a calibration factor C [Bq/cps] for the conversion of the measured cps to activity concentration [Bq/ml] for each voxel j must be applied by eqn. 1.10.

$$q_j = \frac{x_j}{T \cdot V} \cdot C \tag{1.10}$$

This factor is derived from a measurement with the voxel count rate x_j, a known acquisition time T, voxel volume V and activity concentration for each voxel q_j. Together with the above mentioned correction factors thereby a quantitative emission image can be obtained.

1.5   Objectives of this thesis

The aim of this thesis was the investigation and improvement of dosimetry concepts in the image based dosimetry for radioligand therapies using the radionuclide ^{177}Lu.

The first objective was to precisely characterize the time-activity curves of the radiopharmaceutical ^{177}Lu-DOTATATE in the kidneys, which are the major risk organs in this therapy. A robust and feasible model had to be derived for accurate dosimetry based on only few imaging time points, which is the situation in clinical routine.

The second objective was to perform the first image based dosimetric calculations for ^{177}Lu-DKFZ-PSMA-617, a new compound for the radionuclide therapy of prostate cancer. Therefore the modeling of TACs for this unknown tracer dynamic was supported by the findings of the first publication. Furthermore, a modification of the image analysis compared to the previous publication was necessary, since, in addition to the temporal interference, a spatial interference at the kidney region was observed. The latter could be addressed to activity accumulations which superpositioned in the measured planar projection data. The aim of this second study was to establish and utilize 3-D imaging techniques, which are superior to 2-D projection-based techniques for the purpose of separation and delineation of multiple tracer accumulations in an anatomical area.

Chapter 2

Studies

2.1 Preliminary studies for investigation of models with temporal interference

The following section is based on the work DELKER *et al. 2013 in Nuklearmedizin and* DELKER *et al. 2014 in European journal of nuclear medicine and molecular imaging* [16][15].

Besides the specific binding to neuroendocrine tumors during the PRRT with ^{177}Lu-DOTATATE, healthy tissue suffers from tracer accumulation and thus an unwanted irradiation. Especially the kidneys are organs at risk. To estimate the absorbed dose in the kidneys subsequent measurements have to be performed after therapy. Unfortunately the medical condition of these patients is often considerably impaired. Therefore the acquisition of a large number of time points is not appropriate and a reduced number of measurements has to be considered as basis for dosimetric calculations. For this purpose the clinically established full-data model, being comprised of acquisitions at days 1 ($\sim$ 1 h), 2 ($\sim$ 24 h), 3 ($\sim$ 48 h) and 4 ($\sim$ 72 h) after injection, was considered as baseline and compared to reduced-data models in which one of these datapoints was omitted. Then the mean absolute percentage error (MAPE) and the Spearman's rank correlation coefficient (Rho) were calculated from the difference in the estimated absorbed dose. Furthermore, computer simulations of the dose calculation based on the reduced data models were performed to determine the expected deviation from the baseline.

Dosimetric planar image data of 10 patients were acquired on a Siemens E.Cam (Siemens Medical Solutions, Erlangen, Germany) in anterior and posterior projections. Each image was corrected for scatter and attenuation with the triple energy window method and the conjugate view method, respectively [35][24]. Finally images were calibrated using the calculated net activity known for the first time point. The following absorbed dose estimation was then performed according to the MIRD concept with individual scaling for patient mass according to equation 1.4.
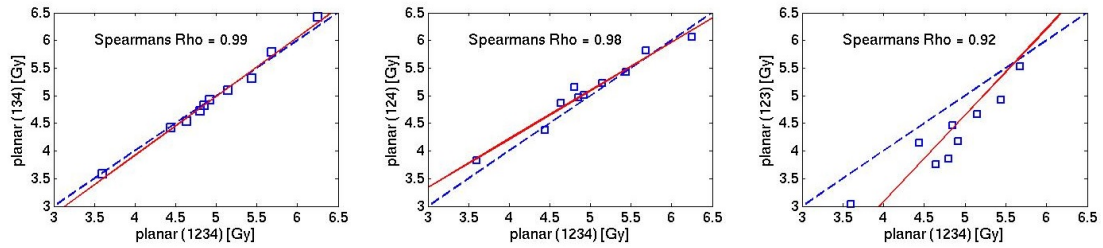
Figure 2.1: Comparison of the dose estimated from planar measurements using all 4 datapoints (1234, horizontal axes) to the case with one time point being omitted (vertical axes). The bisecting lines (dashed line) the linear regression (red line) and the Spearman's Rho values are displayed in each graph.

For the simulations the mean effective half-life and the mean initial activity of the 10 patients were used as a starting point to generate datapoints from a mono-exponential model similar to those chosen in therapy. Additionally, a random noise was sampled from a normal distribution (ND) with a standard deviation σ varied between 5 % and 30 % in 5 %-step intervals (eqn. 2.1):

$$ND(\sigma) = \sigma \cdot 2\sqrt{2ln2} \ \text{ with } \ \sigma = 5, ..., 30\%. \tag{2.1}$$

Afterwards, alternately one of the datapoints was omitted and the remaining points were fitted to a mono-exponential function to calculate the absorbed dose of these reduced data models. In analogy to the patient experiment the resulting dose was compared to the baseline and the MAPE was calculated from 1000 repetitions. This procedure was repeated for an effective half-life range between 1.3 to 3.3 days -with regard to the mean effective half-life of 50.4 h observed in the patient experiment- in steps of 9.6 h.

Comparing the effect of the reduced data models in patient measurements (figure 2.1), only a small deviation and a very strong correlation was observed for the planar measurement 1, 3 and 4 (134) (figure 2.1, left), with a MAPE of 1.3 % and the Spearman's Rho of 0.99 and the measurement days (124) with a MAPE of 3.1 % and a Rho of 0.98 (figure 2.1, middle). By omitting the last measurement (123) an elevated MAPE of 12.6 % and a Rho of 0.92 was determined (figure 2.1, right). No special investigation of the error from the omission the first whole-body measurement (234) compared to the baseline was performed, since its importance to calibrate the planar images.

The simulation of the deviations of the dose estimates from the reduced data models to the baseline resulted in figure 2.2. The surface plots show the mean deviation in dependency of the effective half-life on the x-axis and the relative image error σ (cf. eqn. 2.1) on the y-axis for each case. In contrast to the patient experiment, the configuration without the initial measurement at 1 h p.i. was also simulated (234).

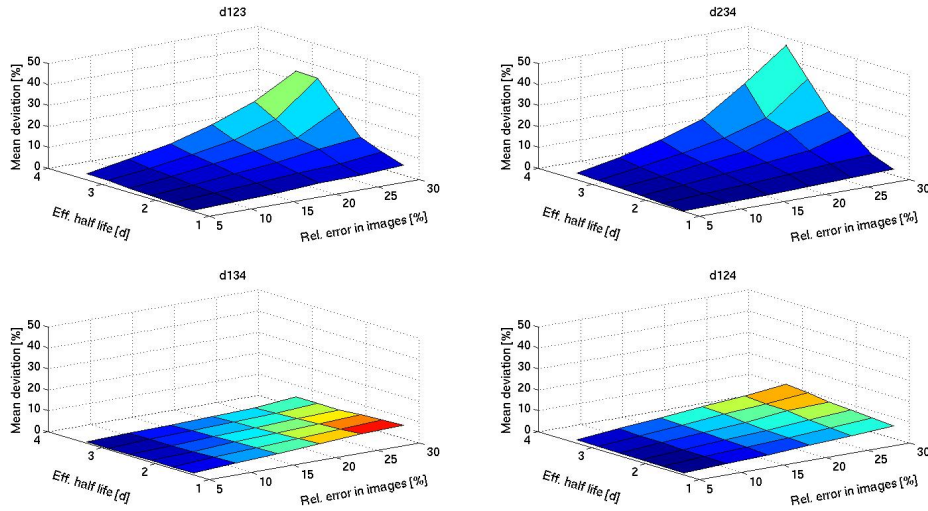Taking into consideration the image errors, which were reported by DERAJAWA et al. to be up

Figure 2.2: Mean deviation [%] of the simulated measurement setup to the baseline (1234) for (123), (234), (134) and (124) each with alternating effective half-life [d] and relative error in the images [%].

to 20 % [21], and the mean effective half-life from the patients of 2.1 d, a MAPE of 3.4 % for simulation (134) and 4.7 % for simulation (124) was calculated. By omitting the first (234) or the last (123) datapoint the MAPE changed to 6.8 % and 6.9 % respectively.

These studies, which were also presented and discussed at the annual meeting of the *European Association of Nuclear Medicine* (EANM 2013) and the meeting of the *Deutsche Gesellschaft für Nuklearmedizin* (DGN 2014) [16][15], offered a good comprehension of the expected deviations if one measurement was canceled due to patient discomfort. No remarkable deviation was stated when omitting one of the middle time points as confirmed via the simulation results. In concordance with LARSSON et al. [40], the deviation increased when excluding the latest time point (fig. 2.2, top left), since this affected the integration to infinity significantly in the calculation of the accumulated activity. In contrast, the increased MAPE which was observed when omitting the first measurement (cf. figure 2.2, top right) was unexpected. Therefore a study for the investigation of this effect was designed, which concludes in the first publication of this thesis: *The Influence of Early Measurements Onto the Estimated Kidney Dose in [^{177}Lu][$DOTA^0, Tyr^3$] Octreotate Peptide Receptor Radiotherapy of Neuroendocrine Tumors* [14].

2.2 Investigation of models with temporal interference

The following section is based on the publication DELKER *et al. 2015 in Molecular imaging and biology and the work* DELKER *et al. 2014 in European journal of nuclear medicine and molecular imaging and* DELKER *et al. 2015 in Nuklearmedizin* [14][19][20].
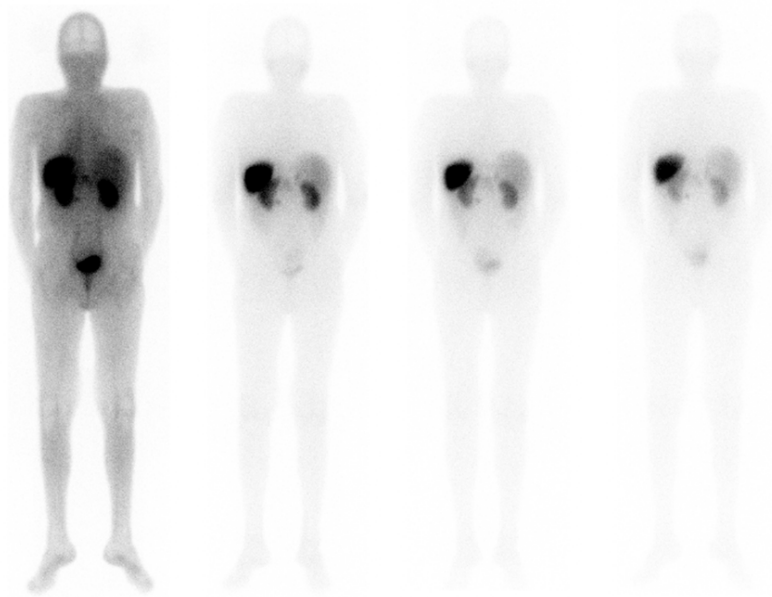
Figure 2.3: Posterior planar whole-body view approx. 1, 24, 48, 72 h (from left to right) after administration of ^{177}Lu-DOTATATE.

The aim of this work was to investigate the influence of early time point measurement in the renal dose calculation by comparing the conventional mono-exponential model to an extended, but in clinical routine unfeasible model and the impact onto the estimated kidney dose in dependence of the measurement dates. Therefore, dynamic planar 1-bed recordings in 12 frames, each 5 min, were acquired in supplement to the conventional whole-body planar scintigraphy images at approx. 1, 24, 48 and 72 h after administration of ^{177}Lu-DOTATATE (see figure 2.3).

A three-phase model with a linear increase to the maximum within the initial minutes post injection (p.i.) followed by a bi-exponential decline served as reference model for evaluating accuracy of the dose estimates compared to the conventional mono-exponential model in 105 patients. The mean effective half-lives of the bi-exponential were 25.8 min $\pm$ 12.0 min for the fast phase and 63.9 h $\pm$ 17.6 h for the slow phase. Then the optimal measurement date was investigated by comparing the deviation to the baseline model of the fit to all four whole-body measurements (4P-fit) or only to the last three (3P-fit). Although various functions were tested by the statistical F-test, the mono-exponential was calculated to be the best suitable. In this study we could show that the first whole-body planar measurement of the kidneys at 1 h has a high probability of being interfered by a second phase which is very likely originating from the remaining blood activity. Consequently the activity at this time is artificially increased,
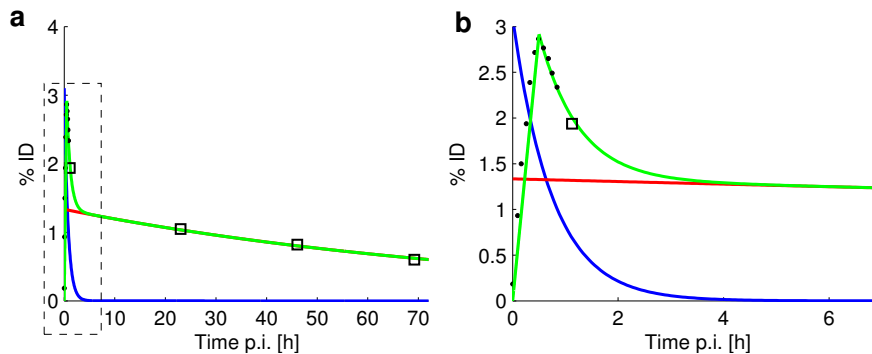
Figure 2.4: (**a**) TAC of the reference TrBi-exp model in green, fitted to the 12 dynamic planar datapoints (filled circles) and the 4 whole-body images (open squares). The single phase fractions of the bi-exponential are plotted in blue and red. (**b**) Expansion of the dashed rectangular in (a) to visualize the first 6 h.

as illustrated in Figure 2.4. There the reference model TrBi-exp is plotted in green onto the dynamic (filled squares) and whole-body (open squares) datapoints. Its two phases, the fast and slow washout phase are depicted separately in blue and red. The first whole-body datapoint at approx. 1.5 h is clearly elevated above the slow washout phase (figure 2.4**b**).

Different than expected this elevated datapoint doesn't result in an increased absorbed dose when using the mono-exponential 4P-fit but in a mean underestimation of 12.4 % $\pm$ 9,2 %, because of a steeper descent of the exponential. This underestimation could lead to a higher administered activity in the next cycle and thus to an overdosage. Whereas the 3P-fit, with the first elevated whole-body excluded, only differs slightly from the reference model. In figure 2.5 these results are summarized for all 105 kidneys.

In this work an underestimation of the dose estimate could be prevented by choosing the appropriate model which is designed to be insensitive to a temporal interference of different phase fractions. Moreover, also a reduction of the workload for patients and staff was achieved without a major loss of accuracy.

2.3 Preliminary studies for investigation of spatial interference

2.3.1 The effect of overlying extra renal activity on estimated renal doses from planar scans

The following section is based on the work DELKER *et al. 2012 in European journal of nuclear medicine and* DELKER *et al. 2014 in Nuklearmedizin* [18][17].
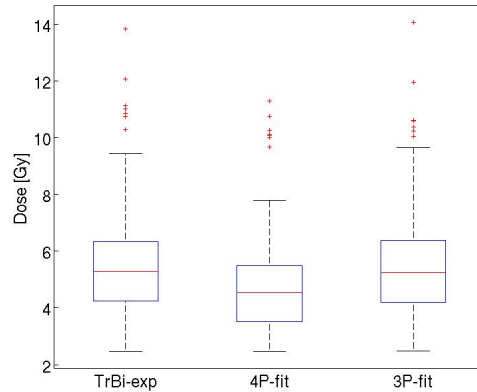
Figure 2.5: Boxplot of the estimated dose calculated for TrBi-exp (left), the four datapoint mono-exponential fit (middle) and the three datapoint mono-exponential fit (right). Outliers are plotted individually (red).

In targeted radiotherapies an accurate and quantitative determination of the regional tracer distribution in the patient is necessary to calculate the absorbed dose. As described before, several imaging modalities are provided for this task in nuclear medicine. Particular planar 2-D gamma camera images are commonly used for therapy images because of their feasibility. A drawback of this method are activity interferences from consecutive activity regions which accumulate in the planar projection to an artificial higher distribution. To improve this impairment a method of extrapolating the mean activity in an overlay-free part of an organ to its whole volume was examined. Furthermore, the more complex 3-D SPECT technology was used to compare and correlate the results of the methods.

To investigate the impact of the correction method onto the dose calculations, 13 patients were measured with anterior and posterior planar images at 1, 24, 48, 72 h after administration of ^{177}Lu-DOTATATE. Subsequently to each planar measurement a 3-D SPECT measurement was acquired at the abdomen. The kidneys, as previously mentioned being one of the organs at risk in this therapy, were examined because of a frequent overlapping of the liver activity distribution onto the activity signal of the right kidney in planar projection data. To compensate for this overlay two separate ROIs were drawn: One to assess the mean accumulation in the overlay free area and the other to specify the organ size. Thereafter, the activity was extrapolated over the entire organ to calculate the residence time (RT) as a surrogate for the absorbed dose. As reference for an overlay free activity-signal the SPECT measurements were utilized. For an objective comparison the Spearman's ρ for correlation and the Mann-Whitney U-test with the probability p for significance were performed [57] [43].

The results of this study which were presented at the EANM 2012 are shown in figure 2.6 [17].
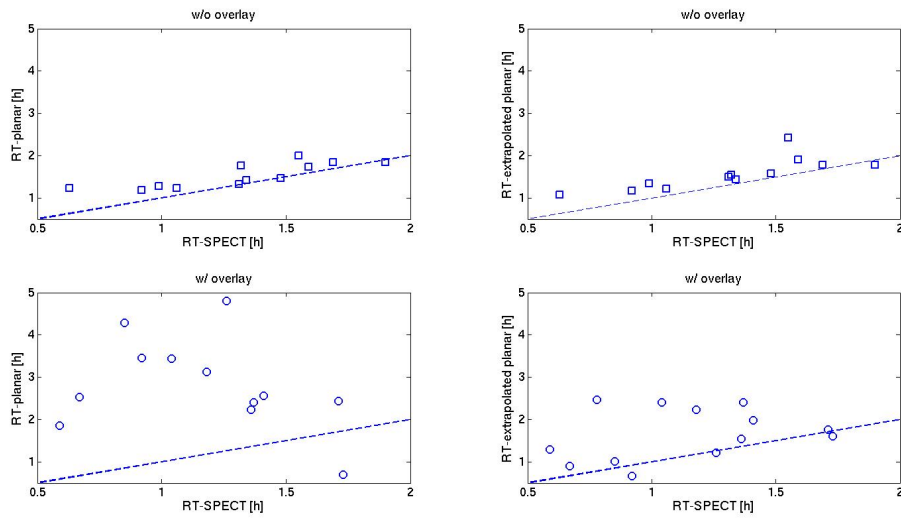
Figure 2.6: Residence times (RT) of the different methods with (bottom row) and without renal overlay (top row)

In the absence of overlay a strong correlation was indicated for the classical planar (Spearman's $\rho = 0.87$) (fig. 2.6, left) and the extrapolated planar method ($\rho = 0.91$) (fig. 2.6, right) in comparison to the SPECT. Also no significant difference was found with the Mann-Whitney U test for the planar method (p = 0.27) with the average residence time of 1.55 ± 0.30 h and for the extrapolated planar method (p = 0.14) with the RT of 1.56 ± 0.37 h, assuming a significance level of 5 %. With overlay of the kidneys no correlation between SPECT and the planar method was found ($\rho = $ -0.37). Also the extrapolated planar method offered no substantial improvement with a ρ of 0.30. The U-test indicated a significant difference between planar and SPECT (p = 0.0002) and extrapolated planar method and SPECT (p = 0.04). Only a small improvement for the mean RT was achieved from 3.43 ± 2.44 h for planar to 1.65 ± 0.61 h with the extrapolated planar method in comparison of 1.14 ± 0.37 h for SPECT.

Without extra renal activity the planar and the correction by extrapolation provided similar results which indicates a general functionality of this method. However, no accordance was found when activity overlay was present. Potentially this arises because of an elevated activity signal next to the superimposed area which results in higher mean values. Because no accurate activity distribution and therefore absorbed dose calculation could be performed if this spatial activity interference is present, a substantial need for a reliable method for activity determination was present. Therefore the focus was directed to the more complex but overlay independent quantitative SPECT, as described in the following sections.

2.4 3-D Dosimetry based on quantitative SPECT for a new therapeutic compound

The following section is based on the publication DELKER *et al. 2015 in European journal of nuclear medicine and molecular imaging and the work* DELKER *et al. 2015 in European journal of nuclear medicine and molecular imaging and* DELKER *et al. 2015 in Journal of nuclear medicine* [13][12][11].

Prostate cancer, one of the most occurring tumors affecting men, tends to become highly aggressive over time and causes the death of more than 250,000 people each year [42]. With the radioligand ^{177}Lu-DKFZ-PSMA-617 a promising new tool for the treatment was developed. To determine the optimal treatment activity to achieve the best therapeutic effect with limited side effects a dosimetry is mandatory. The aim of this study was to perform the first image-based absorbed dose calculations for this new PSMA ligand. To accurately investigate the dose distribution for this new therapeutic approach, we decided to utilize quantitative 3-D SPECT imaging. Quantitative 3-D SPECT images offer a series of advantages over the 2-D planar scintigraphies. Besides the possibility to distinguish between overlapping source distributions, this technique also allows for voxelwise activity determination which enables the calculation of heterogeneous dose maps with the help of convolution or Monte Carlo methods. For the quantification of the SPECT, the image-degrading effects presented in chapter 1.4 have to be compensated. To correct the image for the scattered photons the triple-energy window method, similar to ICHIHARA et al. was utilized [35]. Because of the Compton energy shift in case of an inelastic scatter event (cf. eqn. 1.8), the influence of the scattered photons on the main photopeak window can be offset by acquiring additional adjacent energy windows (cf. figure 2.7). From these, the trapezoidal area in the main photopeak, representing the interspersed photons, is estimated and subtracted by the integral of the linear connection between the measured counts of the two scatter windows.

To compensate the attenuated photon signal described in chapter 1.4, the Hounsfield units of a co-registered CT were converted into a map of linear attenuation coefficients (μ-map). A difficulty in this process is the generation of energy-dependent μ-values for the narrow emission energies of the radionuclides from the broad polychromatic X-ray spectrum. Hence the CT system with the operating voltage of 130 kVpeak was characterized with the Gammex 467 tissue characterization phantom (Gammex, Inc.) shown in the insert of figure 2.8. Then, because of the known material composition of the phantom rods, conversion factors from the CT Hounsfield units to linear attenuation coefficients could be derived for the desired energies. The μ-values for the corresponding radionuclide energies of one mixture were obtained from the database of the *National Institute of Standards and Technology* (NIST) [44], by summing up the weighted atomic constituents i:
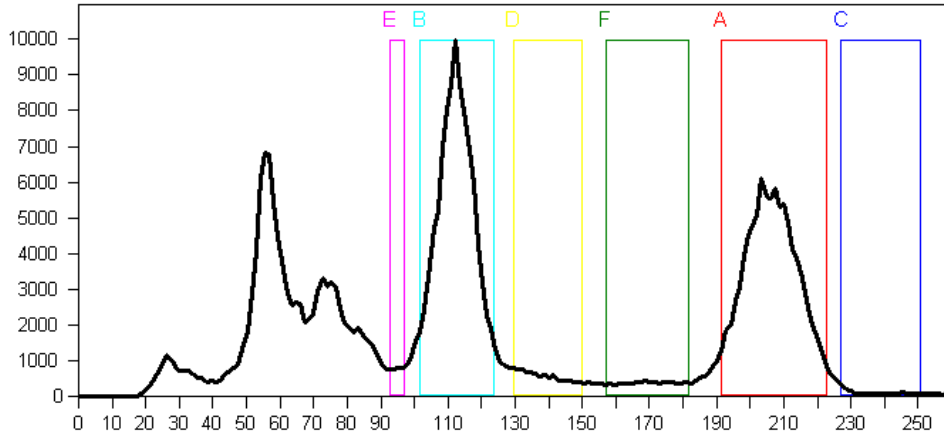
Figure 2.7: Energy spectrum with photopeak (A and B) and scatter (C to F) windows transcribed during a SPECT measurement with ^{177}Lu. The scales are measured counts on the y-axis and energy in keV on the x-axis.

$$\frac{\mu}{\rho} = \sum_i w_i (\frac{\mu}{\rho})_i. \tag{2.2}$$

As an example in figure 2.8 the bi-linear plots for the conversion of HU to the two main ^{177}Lu photopeak energies are plotted. At this point it should be noted, that both photopeaks were acquired in the measurements of this work (also compare figure 2.7), but only the upper energy peak at 208 keV was processed for image reconstruction. In general, the count statistics in therapy images with ^{177}Lu is sufficient, but if deemed necessary also the lower peak at 113 keV could be additionally processed.

Finally, a model was included in the reconstruction algorithm to describe the distance dependent detector response. Therefore a point source of ^{177}Lu was measured at different distances of the detector head, which was equipped with a medium energy collimator. The measured signal of the point source was fitted to a gaussian function to derive a distant dependent model of the point spread function (PSF). Consequently, with the PSF included in the system matrix of the reconstruction and the distance from the detector, which is obtainable from the image header, a resolution recovery could be achieved. In this work no dedicated corrections were applied for deadtime, partial volume effects and spill-over. The applied image reconstruction was "a rotation-based one-step-late penalized ordered subsets expectation maximization algorithm" [11]. In our featured publication (DELKER et al.) it is "*described by equation [...][2.3],*

$$x_j^{k+1} = x_j^k \frac{1}{\sum_{i \in S_n} a_{ij} + \beta\left(P(x_j^k)\right)} \sum_{i \in S_n} a_{ij} \frac{y_i}{(\sum_j a_{ij} x_j^k) + s_i} \tag{2.3}$$

where $P(x_j^k)$ denotes a quadratic filter operation onto voxel j using its $5 \times 5 \times 5$ neighboring voxels, and S_n is the subset of projections to be considered. A penalty weight factor β was of low
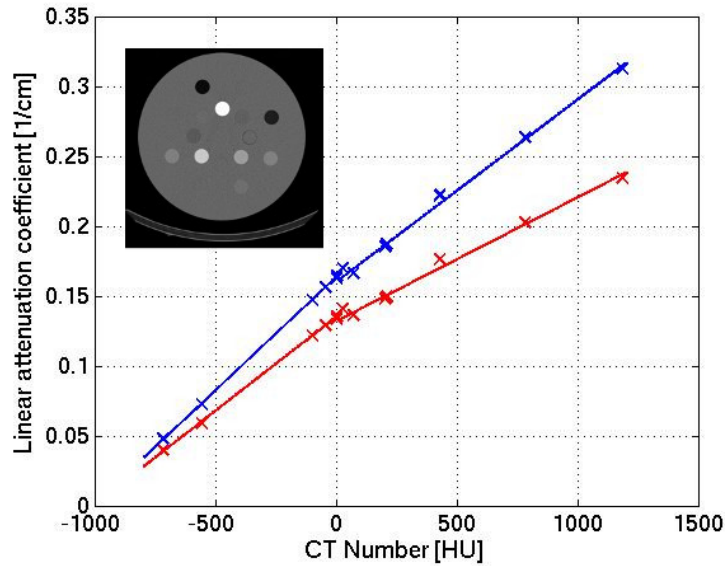
Figure 2.8: Bi-linear conversion graph from CT Hounsfield units to linear attenuation coefficients (per cm). The known phantom rod μ values were plotted to the measured CT Hounsfield units for the main ^{177}Lu photopeaks at 208 keV (red) and 113 keV (blue).The insert in the left upper corner shows the CT image of the used Gammex 467 characterization phantom.

magnitude in order to slightly reduce the Gibbs artefacts without greatly sacrificing resolution. According to [. . .][eq. 2.3], the final image x^k after iteration k contained the number of reconstructed counts per voxel. Quantitative emission images, obtained as activity concentration per unit volume (i.e. q in Becquerels per millilitre) in each voxel j, were then calculated" with the calibration factor C by equation 1.10 [11]. This factor was determined by a separate measurement of a cylindric calibration phantom with known activity and yielded a C of 110,058 Bq/cps.

The effect of the presented image corrections with applied calibration factor are exemplified in the NEMA-NM-2001 phantom measurement shown in figure 2.9. Therefore six spheres of internal diameters of 37 mm, 28 mm, 22 mm, 17 mm, 13 mm and 10 mm were filled with an activity concentration of 75.6 kBq/mL of ^{177}Lu-solution in water. Moreover an activity concentration of 7.5 kBq/mL was mixed in the background, resulting in an foreground-to-background ratio of approximately 10:1. In figure 2.9, the corrections applied for the reconstruction are abbreviated with **a** for **a**ttenuation correction, **s** for **s**catter correction and **b** for distance dependent detector **b**lur. Here, the need for compensating the image degrading factors becomes apparent. Without any corrections (a0s0b0), the recovery coefficient (RC) of the background was 26 % (cf. figure 2.10(b)). Moreover, high image noise, identifiable by the large error bar, was present. By applying the appropriate model for the distance detector blurring (a0s0b1), the noise is canceled out and the edges of the spheres become more defined (cf. figure 2.9(b)). However the RC did not change substantially, displayed by the blue bar in figure 2.10(b). If the scatter correction is

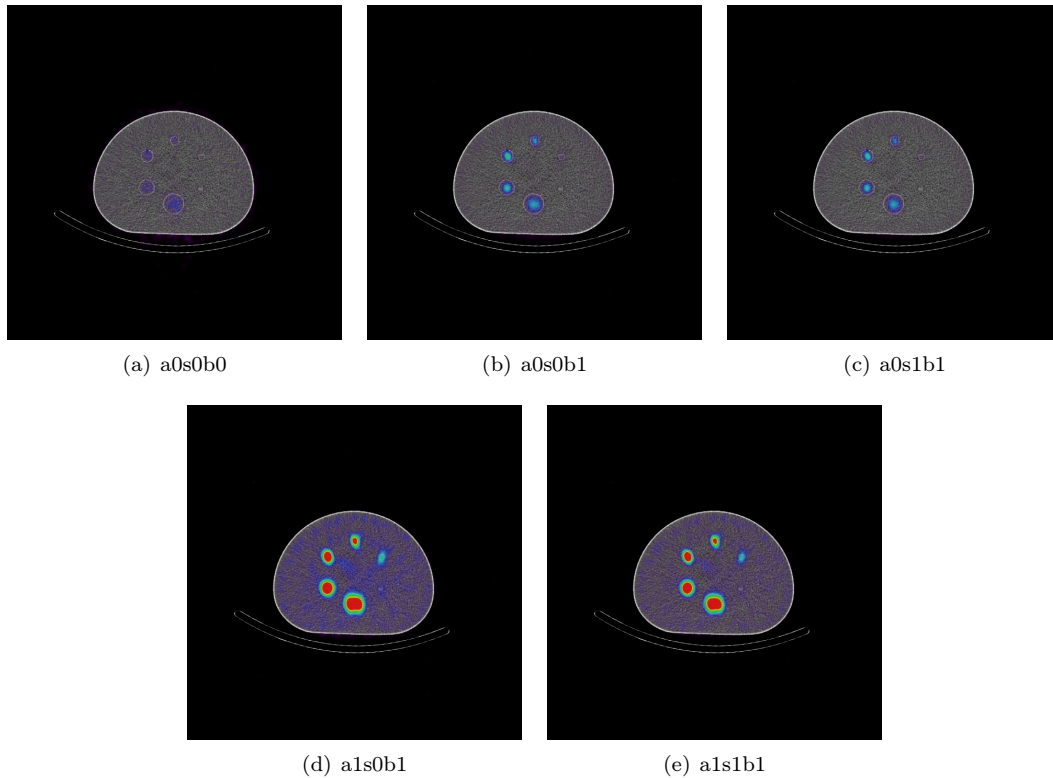(a) a0s0b0 (b) a0s0b1 (c) a0s1b1

(d) a1s0b1 (e) a1s1b1

Figure 2.9: Reconstructed images of a NEMA 2001 phantom with hot spheres and background activity. The corrections performed are abbreviated with **a** for **a**ttenuation correction, **s** for **s**catter correction and **b** for distance dependent detector **b**lur, followed by the digit 1 if performed and 0 if not, respectively.

performed in addition (a0s1b1), the overall signal is even reduced further because of the subtraction of the interspersed photons in the photopeak. The effect of the attenuation compensation (a1s0b1) is illustrated by the significant increase of the RC, which even overcorrects the signal to 128%. Finally, by considering all correction factors (a1s1b1) the RC reaches 93 %. Apparently the activity recovery of the spheres (figure 2.10(a)) with all corrections (a1s1b1) is below the background RC. Moreover, it decreases with sphere size from 81 % for 37 mm diameter to a disappearance in the background noise (approx. 12 %) for the smallest sphere with 10 mm. This most likely originate of the inherent spatial resolution of the SPECT system and the absence of compensation for partial volume effects.

Five patients were treated in two cycles with 3.7 GBq ^{177}Lu DKFZ-PSMA-617. To estimate the accumulated activity of the tumors and organs, planar and SPECT images were recorded at 1 h, 24 h, 48 h and 72 h post injection. Moreover, blood samples were collected for bone marrow dosimetry.

(a) Recovery coefficients of spheres
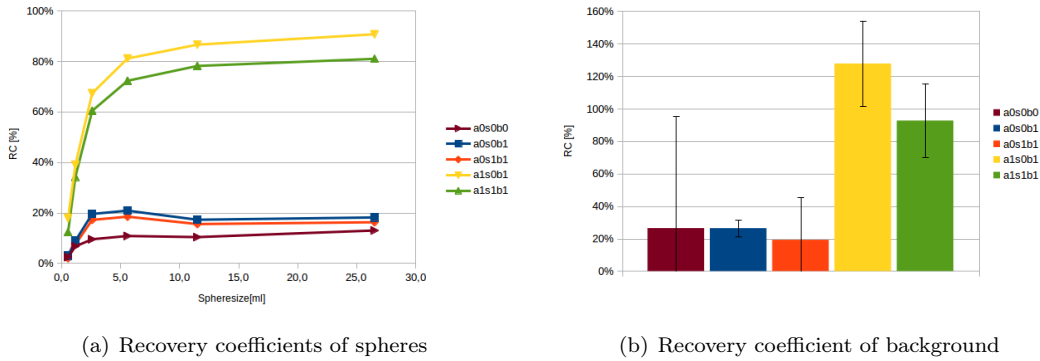
(b) Recovery coefficient of background

Figure 2.10: Recovery coefficients (RC) calculated from the NEMA 2001 phantom images shown in 2.9, with the same abbreviations. (a) RC calculated for each sphere size. (b) RC calculated for the 784 mL background VOI. The different colors in both figures distinguish between the correction methods applied.
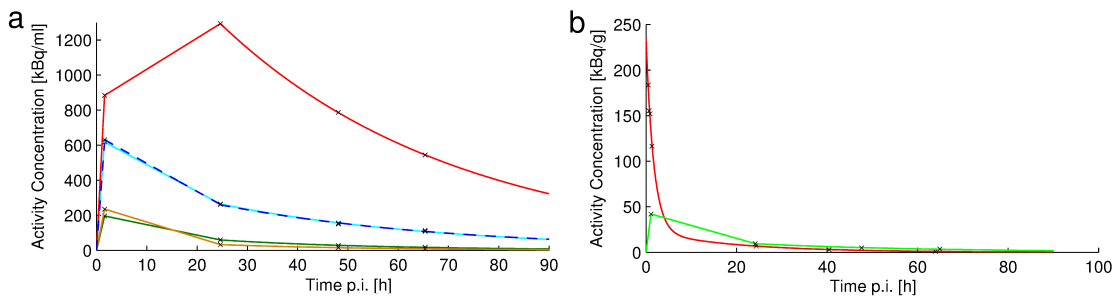

Figure 2.11: **a** Dose model curves of activity concentrations in a representative patient in one tumor metastasis (red), kidneys (cyan and dashed blue), spleen (orange) and liver (green). **b** Activity concentration curves from the blood samples (red) and the whole-body (green) for calculation of the bone marrow dose.

The time-activity curves for the organs and tumors were modeled with multiple distinct phases due to the experiences and results of the previous work (cf. figure 2.11). After approximately 24 h an increased uptake in the intestine was observed which superimposed the kidneys in the planar scintigraphies (figure 2.12). Due to this spatial interference the overlay-free quantitative 3-D SPECT images were utilized for the dosimetry calculations of the abdominal organs (figure 2.13). The bone marrow was estimated from a combination of the blood sampling method and image data, presented in section 1.2.2. Thereby the remainder of the body was calculated by the accumulated activity from the whole-body planar images, minus the activity of the organs and the blood. The estimated absorbed bone marrow dose was 12 mGy/GBq per cycle.

Besides the tumor the highest absorbed dose estimates were observed in the kidneys (0.6 Gy/GBq) and the salivary glands (1.4 Gy/GBq), however both absorbed dose values are not critical considering the administered activity of 3.7 GBq. Furthermore, the liver and the spleen
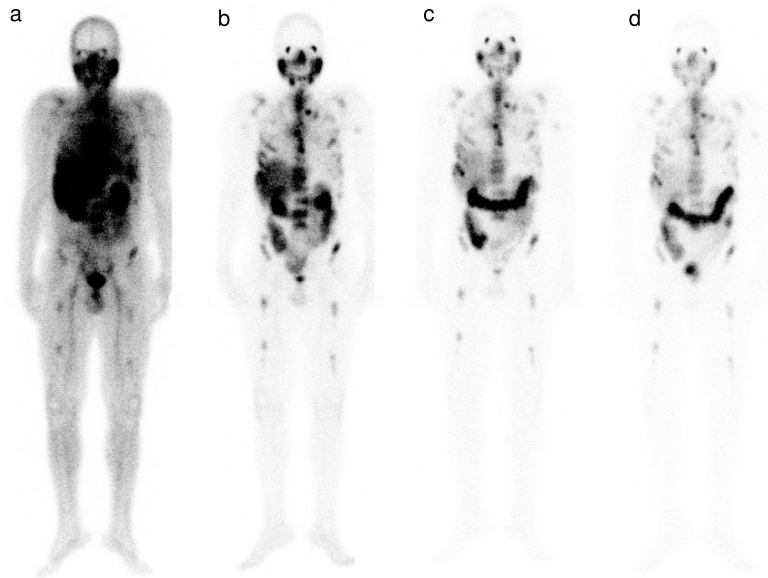
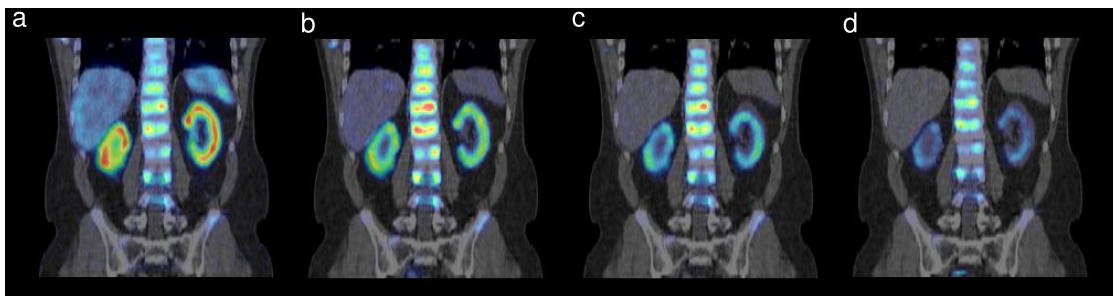Figure 2.12: Anterior planar whole-body images at **(a)** 1, **(b)** 24, **(c)** 48 and **(d)** 72 h.

Figure 2.13: Serial fused SPECT/CT coronal images at **(a)** 1, **(b)** 24, **(c)** 48 and **(d)** 72 h.

received a considerably low dose of 0.1 Gy/GBq each. Consequently we recommended a more aggressive treatment, starting with an administered activity of 6.0 GBq to optimally exploit the absorbed tumor dose.

Chapter 3

Discussion

In this work, therapy images for dosimetry of ^{177}Lu-labeled tracers were investigated for temporal and spatial effects. In the first study, the multi-phase kinetic of the tracer ^{177}Lu-DOTATATE was investigated.

Although a single-phase mono-exponential model proved to be sufficient for dose estimations with only small deviations of a few percent from the best model, we observed that this mono-exponential model is highly sensitive to the appropriate selection of data to be fitted. By choosing a set of inappropriate time points a mean underestimation of dose of 12.4 % $\pm$ 9.2 % was noted. Assuming multiple therapy cycles, the danger of a substantial overexposure of the risk organ is present. Due to the measurement of a large set of time points and the assessment of the pharmacokinetics using multi-phase models, this effect could be addressed to the temporal interference of fast and slow pharmacokinetic phases. Consequently, the assumed initial model for the performed simulations of the preliminary studies in chapter 2.1 inadequately described the true temporal activity distribution. By adapting and repeating the simulations, new surface plots of the mean deviation were calculated (figure 3.1).

In this simulations a model for multiphase kinetics with linear increase and bi-exponential washout was included to describe the baseline to which in analogy to the simulations of figure 2.2 the reduced whole-body setup was analyzed. Comparable to the results of the first publication [14], the omission of the first measurement (d234) (figure 3.1, top right) causes only a minor deviation to the baseline of approximately 1 %, assuming 48 h effective half-life and an image error of 20 %. With the inclusion of the influenced first measurement (figure 3.1, top left and bottom row) an increased deviation of 11 % for (d123) and 8 % for (d134) and (d124) was observed. This simulation confirms the finding of the publication, that almost the entire dose (98.9 %) is caused by the slow phase component and an accurate determination of the slow phase could therefore be sufficient to characterize the dose. Hence, the fit to the datapoints of the mono-exponential function were adapted with omission of the measurements at therapy day to avoid the risk of temporal interference effects. This enabled an improved calculated absorbed
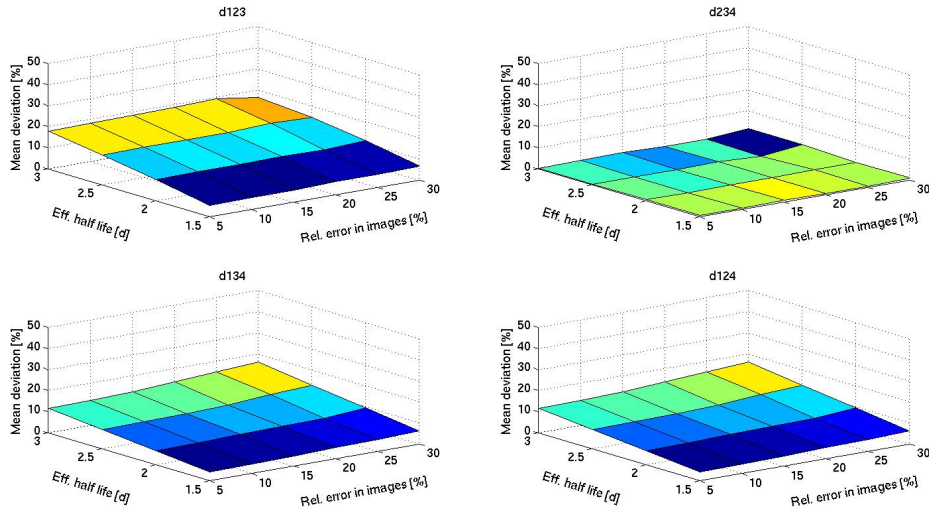
26

Figure 3.1: Mean deviation of the simulated measurement setup to the adapted baseline with linear increase to the maximum, followed by a bi-exponential function. In analogy to 2.1 the effective half-life and the relative error in the images was altered.

dose with supplemental minimization of the work load for staff and patients.

In order to compensate spatial interference effects, which occur in planar therapy images, two methods were investigated. At first, we studied a method of extrapolating an overlay free activity region over the whole organ (cf. section 2.3). As a proof of principle, this method was tested with overlay free kidneys and showed good correlations. But with overlay no significant improvement could be achieved, potentially because of an elevated activity signal in the surrounding of the superimposed area. Because these attempts have not been successful, quantitative 3-D SPECT was established and optimized for the dose calculation in our department. Therefore a phantom measurement was performed to evaluate this method. For the spheres with a volume greater than 10 mL a recovery coefficient of approximately 80 % was determined, which is in good accordance to a recent study of ^{177}Lu SPECT quantification [49]. The decrease of the RCs with sphere size "most likely arose from inherent spatial resolution, with signals uncorrected for partial volume and spill-over effects" [11]. Because dosimetry is mostly performed to estimate the dose to the larger risk organs, no special need to include these corrections was present. However, the tumor dose assessment is affected and the implementation of these corrections should be considered. Moreover, no dead time correction was included in the SPECT workflow yet. In the study of the new PSMA compound [11], a relatively low therapy activity of 3.7 GBq was administered. Therefore, no substantial dead time error was expected. Furthermore, in this study we observed an activity signal in the intestine which overlapped significantly with the kidneys in planar scintigraphies (cf. figure 2.12). That made the application of SPECT-based 3-D dosimetry indispensable. With the choice of the appropriate model and the compensation
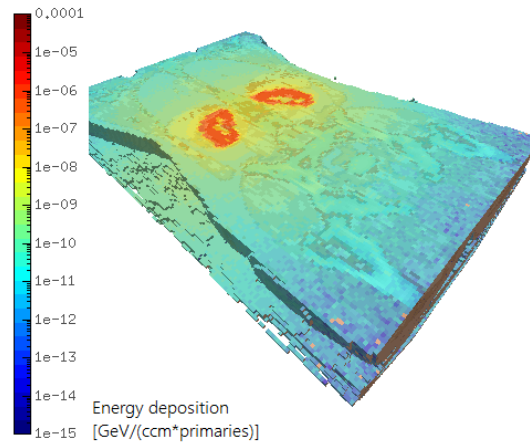
Figure 3.2: Simulation geometry and total energy deposition of the FLUKA Monte Carlo code. The CT body data was overlayed by the estimator results for total energy. Image taken from [29].

of spatial interference effects due to the application of the 3-D SPECT imaging, first reliable dose estimates could be determined for this new therapeutic compound. To avoid the fitting of a one-phase model to a temporal interfered measurement of multiple phases, the first datapoint was excluded from the fit but instead interpolated linearly (cf. fig. 2.11).

The calculated absorbed doses for ^{177}Lu-PSMA with this model were 0.6 Gy/GBq for the kidneys, 0.1 Gy/GBq for the liver and 0.1 Gy/GBq for the spleen. The kidneys, being the dose limiting organ in a number of radionuclide therapies [8][38], received the highest dose amongst the evaluated abdominal organs. Nevertheless the dose is comparable to the well established ^{177}Lu-DOTATATE therapy, which was published previously [50]. With the help of the whole-body planar scintigraphy, the mean absorbed dose to the salivary gland was determined to be 1.4 Gy/GBq. Nevertheless, no patient complained of xerostomia during the follow-up. Furthermore, from external beam therapy a dose of 30 to 40 Gy was reported to be critical [26][32], which was not reached in any patient during the treatment with ^{177}Lu-DKFZ-PSMA-617. The bone marrow, which is critical in other targeted radionuclide therapies [25][39][54][52], was estimated to absorb a dose of 12 mGy/GBq. This is well below the critical level of 2 Gy [25]. Nevertheless, the utilized model for bone marrow calculation did not take into account the high amount of activity near or within the red marrow because of the variety of bone metastasis. Because no critical organ dose was observed in the therapy of this new treatment option for patients with metastasized castration resistant prostate cancer, a more aggressive treatment activity could be suggested.
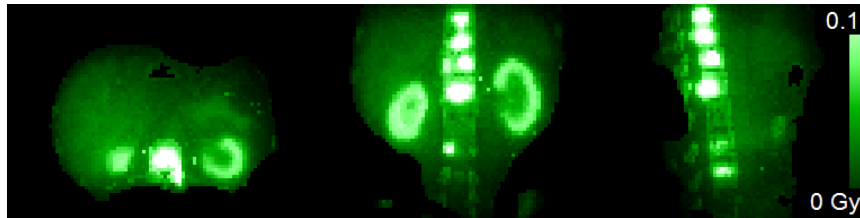
As emphasized in section 1.2, only minor corrections for patient individual scaling are performed
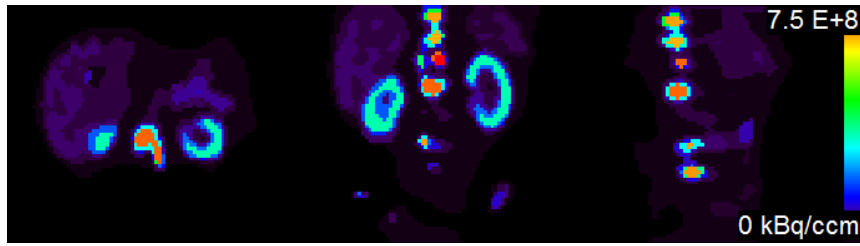
(a) Map of accumulated activities
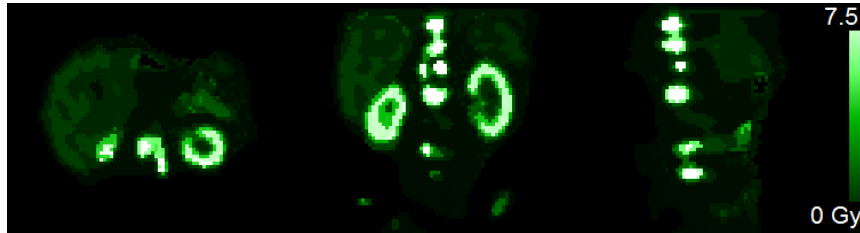
(b) FLUKA 3-D total absorbed dose

(c) FLUKA 3-D photon dose

Figure 3.3: Monte Carlo based 3-D patient study with ^{177}Lu-PSMA. (a) Patient specific map of accumulated activities. (b) Simulated 3-D dose map in [Gy]. (c) Photon dose contribution of the dose. The images were taken from [29].

with the MIRD S-value dose estimation. For more patient specific calculations, the dose distribution in the true anatomical patient geometry would be desirable. In this matter, a brief outlook of the preliminary results of direct Monte Carlo simulations and convolution methods with dose point kernels is presented in the following paragraph.

The Monte Carlo simulation is regarded as the most precise and patient specific method to calculate the absorbed dose [21]. To determine the energy deposition in the patient via MC, the simulation geometry with the material composition is required, which was obtained by the conversion of Hounsfield units as proposed by SCHNEIDER et al. [51]. Together with the accumulated activity derived from the 3-D SPECT images, which served as source input map, the energy deposition in the patient could be simulated as shown in figure 3.2 using the MC code FLUKA [4]. As an example, figure 3.3 shows a PSMA patient simulated with FLUKA. Furthermore, the MC simulation enables the possibility to investigate special characteristics of the isotope, for example the contribution of the photon energy deposition to the absorbed
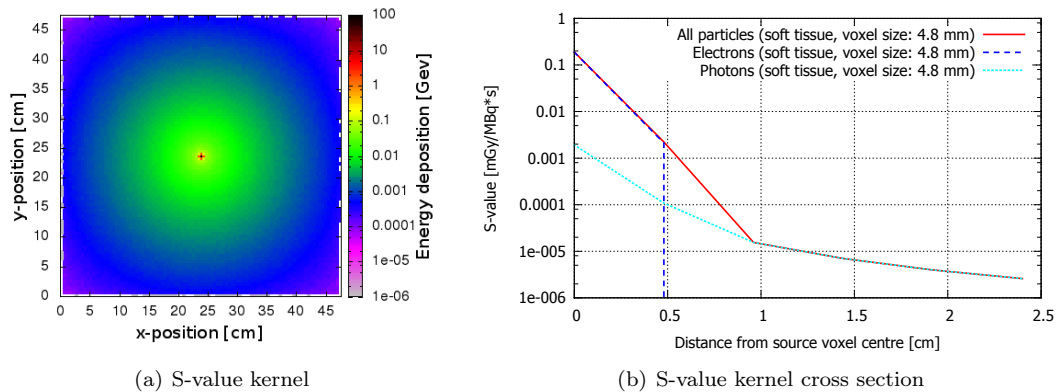
(a) S-value kernel

(b) S-value kernel cross section

Figure 3.4: ^{177}Lu-specific S-value kernels simulated for 4.8 mm^3 soft tissue voxels. The images were taken from [29].

dose in figure 3.3(c), which causes approx. 1 % of the dose for ^{177}Lu. A drawback of this method is the time-consuming simulation process. An alternative to full MC calculations are pre-calculated dose point kernels. These are simulated for representative tissue types such as a kernel for soft-tissue depicted in figure 3.4. These kernels then can be scaled via the CT density and convolved with the activity distribution to obtain the absorbed dose map. Especially in regions where the majority of the energy deposition originate from photons, these methods could improve the accuracy of the dose estimation.

As noted earlier, due to the high amount of activity near or in the bones, a higher absorbed dose to the red marrow is expected. To assess the additional absorbed dose caused by these activities, the latter introduced methods for 3-D dosimetry were applied. At the annual conference of the EANM 2015 ([30]), we indicated a notably dose contribution from the metastasis to the bone marrow of up to 41 % as calculated with MC simulations. Nevertheless the magnitude of the total dose was still below the commonly applied constraints. Furthermore, no harmful influence of other source regions onto the RM was detected.

With the studies and the related publications, which have been summarized in this thesis, some of the major tasks of dosimetry calculation were addressed. It could be shown, that carefully determined models which avoid temporal and spatial interference effects improve the calculation of the absorbed dose and are even suitable to reduce the burden for patients and the work load for the staff. Consequently, with these findings, an accurate dose risk assessment of the new radiopharmaceutical for the treatment of metastasized castration resistant prostate cancer was achieved. Furthermore, the models developed in this thesis serve as a robust input to even more sophisticated approaches such as Monte Carlo simulations or dose kernel convolutions for voxel-

wise investigation of the regional distribution of radiation exposure and dose assessment in well established and innovative prospective radioligand therapies.

Chapter 4

Bibliography

[1] H. O Anger. "Scintillation camera". In: *Review of scientific instruments* 29.1 (1958), pp. 27–33.

[2] D. L Bailey and K. P Willowson. "An evidence-based review of quantitative SPECT imaging and potential clinical applications". In: *Journal of Nuclear Medicine* 54.1 (2013), pp. 83–89.

[3] DL Bailey, JL Humm, A Todd-Pokropek, and A van Aswegen. "Nuclear Medicine Physics: A Handbook for Teachers and Students. Endorsed by: American Association of Physicists in Medicine (AAPM), Asia–Oceania Federation of Organizations for Medical Physics (AFOMP), Australasian College of Physical Scientists and Engineers in Medicine (ACPSEM), European Federation of Organisations for Medical Physics (EFOMP), Federation of African Medical Physics Organisations (FAMPO), World Federation of Nuclear Medicine and Biology (WFNMB)". In: (2014).

[4] G. Battistoni, F Cerutti, A Fasso, A Ferrari, S Muraro, J Ranft, S Roesler, and PR Sala. "The FLUKA code: Description and benchmarking". In: *Hadronic Shower Simulation Workshop(AIP Conference Proceedings Volume 896)*. Vol. 896. 2007, pp. 31–49.

[5] R. P. Baum and H. R. Kulkarni. "THERANOSTICS: From Molecular Imaging Using Ga-68 Labeled Tracers and PET/CT to Personalized Radionuclide Therapy - The Bad Berka Experience". In: *Theranostics* 2.5 (2012), pp. 437–47.

[6] M.-M. Bè, V. Chistè, C. Dulieu, E. Browne, V. Chechev, N. Kuzmenko, R. Helmer, A. Nichols, E. Schönfeld, and R. Dersch. *Table of Radionuclides (Vol. 2 - A=151 to 242)*. Bureau International des Poids et Mesures, Pavillion de Breteuil, F-92310 Sèvres., 2004.

[7] V Bettinardi, L Presotto, E Rapisarda, M Picchio, L Gianolli, and MC Gilardi. "Physical performance of the new hybrid PET/CT Discovery-690". In: *Medical physics* 38.10 (2011), pp. 5394–5411.

[8] L. Bodei, M. Cremonesi, C. M Grana, M. Chinol, S. M Baio, S. Severi, and G. Paganelli. "Yttrium-labelled peptides for therapy of NET". In: *European journal of nuclear medicine and molecular imaging* 39.1 (2012), pp. 93–102.

[9] A. K Buck, S. Nekolla, S. Ziegler, A. Beer, B. J Krause, K. Herrmann, K. Scheidhauer, H. Wester, E. J Rummeny, M. Schwaiger, et al. "Spect/Ct". In: *Journal of Nuclear Medicine* 49.8 (2008), pp. 1305–1319.

[10] S. R Cherry. "Multimodality imaging: Beyond pet/ct and spect/ct". In: *Seminars in nuclear medicine*. Vol. 39. 5. Elsevier. 2009, pp. 348–353.

[11] A. Delker, W. Peter Fendler, C. Kratochwil, A. Brunegraf, A. Gosewisch, F-J. Gildehaus, S. Tritschler, C. G Stief, K. Kopka, U. Haberkorn, P. Bartenstein, and G. Böning. "Dosimetry for Lu-177-DKFZ-PSMA-617: a new radiopharmaceutical for the treatment of metastatic prostate cancer". In: *European journal of nuclear medicine and molecular imaging* 43 (1 2015), pp. 42–51.

[12] A. Delker, W. Fendler, A. Brunegraf, A. Gosewisch, F-J. Gildehaus, P. Bartenstein, and G. Böning. "Dosimetry of Lu-177 DKFZ-PSMA-617 for the treatment of metastatic prostate cancer using quantitative SPECT/CT". In: *European journal of nuclear medicine and molecular imaging*. Springer, 2015.

[13] A. Delker, W. Fendler, A. Brunegraf, A. Gosewisch, F-J. Gildehaus, P. Bartenstein, and G. Böning. "Dosimetry of Lu-177 DKFZ-PSMA-617 for the treatment of metastatic prostate cancer using quantitative SPECT/CT". In: *Journal of Nuclear Medicine* 56.supplement 3 (2015), p. 112.

[14] A. Delker, H. Ilhan, C. Zach, J. Brosch, F. J. Gildehaus, S. Lehner, P. Bartenstein, and G. Boning. "The Influence of Early Measurements Onto the Estimated Kidney Dose in [177Lu][DOTA0, Tyr3] Octreotate Peptide Receptor Radiotherapy of Neuroendocrine Tumors". In: *Molecular Imaging and Biology* 17 (5 2015), pp. 726–734.

[15] A. Delker, C. Zach, H. Ilhan, P. Bartenstein, M. Hacker, A. Haug, and G. Böning. "Der Effekt ausgelassener Messpunkte bei der Nierendosisbestimmung aus planaren und SPECT Aufnahmen nach der Radiopeptid-Therapie mit Lu-177-DOTATATE". In: *Nuklearmedizin*. Thieme, 2014.

[16] A. Delker, C. Zach, H. Ilhan, P. Bartenstein, M. Hacker, A. Haug, and G. Böning. "The effect of omitting measurement points in the estimation of renal doses from planar and SPECT scans after peptide radionuclide receptor therapy using Lu-177-DOTATATE." In: *European journal of nuclear medicine and molecular imaging*. Springer, 2013.

[17] A. Delker, C. Zach, H. Ilhan, P. Bartenstein, M. Hacker, A. Haug, and G. Böning. "The effect of overlying extra-renal uptake on estimated renal doses from planar scans after peptide radionuclide receptor therapy using Lu-177-DOTATATE." In: *European journal of nuclear medicine and molecular imaging*. Springer, 2012.

[18] A. Delker, C. Zach, H. Ilhan, P. Bartenstein, M. Hacker, A. Haug, and G. Böning. "Über-lagerungseffekte bei der Nierendosisbestimmung in planaren Szintigrafien nach der Radiopeptidtherapie mit Lu-177-DOTATATE". In: *Nuklearmedizin*. Thieme, 2014.

[19] A. Delker, C. Zach, H. Ilhan, J. Brosch, S. Lehner, P. Bartenstein, and G. Böning. "Investigation of the influence of early measurement points onto the kidney dosimetry in Lu-177-DOTATATE PRRT". In: *European journal of nuclear medicine and molecular imaging*. Springer, 2014.

[20] A. Delker, C. Zach, H. Ilhan, J. Brosch, S. Lehner, P. Bartenstein, and Böning G. "Untersuchung der frühen Nierenkinetik bei der Lu-177-DOTATATE Radiopeptid Therapie". In: *Nuklearmedizin*. Thieme, 2015.

[21] Y.K. Dewaraja, E.C. Frey, G. Sgouros, A.B. Brill, P. Roberson, P.B. Zanzonico, and M. Ljungberg. "MIRD pamphlet No. 23: quantitative SPECT for patient-specific 3-dimensional dosimetry in internal radionuclide therapy". In: *Journal of Nuclear Medicine* 53.8 (2012), pp. 1310–25.

[22] P. A. Feller, V. J. Sodd, and J. G. Kereiakes. "Using the S tables of MIRD Pamphlet 11". In: *Journal of Nuclear Medicine* 18.7 (1977), p. 747.

[23] J. Ferlay, I. Soerjomataram, R. Dikshit, S. Eser, C. Mathers, M. Rebelo, D. M. Parkin, D. Forman, and F. Bray. "Cancer incidence and mortality worldwide: sources, methods and major patterns in GLOBOCAN 2012". In: *International Journal of Cancer* 136.5 (2015), E359–E386.

[24] J. S. Fleming. "A technique for the absolute measurement of activity using a gamma camera and computer". In: *Physics in medicine and biology* 24.1 (1979), pp. 176–180.

[25] F. Forrer, E. P Krenning, P. P Kooij, B. F Bernard, M. Konijnenberg, W. H Bakker, J. JM Teunissen, M. de Jong, K. van Lom, W. W de Herder, et al. "Bone marrow dosimetry in peptide receptor radionuclide therapy with [177Lu-DOTA0, Tyr3] octreotate". In: *European journal of nuclear medicine and molecular imaging* 36.7 (2009), pp. 1138–1146.

[26] M. F Gensheimer, J. J Liao, A. S Garden, G. E Laramore, U. Parvathaneni, et al. "Submandibular gland-sparing radiation therapy for locally advanced oropharyngeal squamous cell carcinoma: patterns of failure and xerostomia outcomes". In: *Radiat Oncol* 9 (2014), p. 255.

[27] H. U Gerth, K. U Juergens, U. Dirksen, J. Gerss, O. Schober, and C. Franzius. "Significant benefit of multimodal imaging: PET/CT compared with PET alone in staging and follow-up of patients with Ewing tumors". In: *Journal of Nuclear Medicine* 48.12 (2007), pp. 1932–1939.

[28] A. Ghosh and W. D. Heston. "Tumor target prostate specific membrane antigen (PSMA) and its regulation in prostate cancer". In: *Journal of cellular biochemistry* 91.3 (2004), pp. 528–539.

[29] A. Gosewisch. *Dosimetry in Lu-177-Radionuclide Therapy Using Monte Carlo Simulations*. Master thesis, Ludwig-Maximilians University Munich, Munich, 2015.

[30] A. Gosewisch, A. Delker, L. Vomacka, WP. Fendler, A. Brunegraf, FJ. Gildehaus, A. Mairani, K. Parodi, PA. Bartenstein, and G. Boening. "Estimation of local photon dose to active bone marrow in Lu-177 PSMA PRRT therapy using patient-specific Monte Carlo simulations". In: *European journal of nuclear medicine and molecular imaging*. Vol. 42. Springer. 2015, S754–S755.

[31] J. Grimes and A. Celler. "Comparison of internal dose estimates obtained using organ-level, voxel S value, and Monte Carlo techniques". In: *Med Phys* 41.9 (2014), p. 092501.

[32] J. Hey, J. Setz, R. Gerlach, M. Janich, G. Hildebrandt, D. Vordermark, C. R Gernhardt, and T. Kuhnt. "Parotid gland-recovery after radiotherapy in the head and neck region–36 months follow-up of a prospective clinical study". In: *Radiat Oncol* 6 (2011), p. 125.

[33] C. Hindorf, G. Glatting, C. Chiesa, O. Linden, G. Flux, and Eanm Dosimetry Committee. "EANM Dosimetry Committee guidelines for bone marrow and whole-body dosimetry". In: *European journal of nuclear medicine and molecular imaging* 37.6 (2010), pp. 1238–1250.

[34] H. M. Hudson and R. S. Larkin. "Accelerated image reconstruction using ordered subsets of projection data". In: *Medical Imaging, IEEE Transactions on* 13.4 (1994), pp. 601–609.

[35] T. Ichihara, K. Ogawa, N. Motomura, A. Kubo, and S. Hashimoto. "Compton scatter compensation using the triple-energy window method for single- and dual-isotope SPECT". In: *Journal of Nuclear Medicine* 34.12 (1993), pp. 2216–21.

[36] BW Jakoby, Y Bercier, M Conti, ME Casey, B Bendriem, and DW Townsend. "Physical and clinical performance of the mCT time-of-flight PET/CT scanner". In: *Physics in medicine and biology* 56.8 (2011), p. 2375.

[37] R. T Jensen, G. Cadiot, M. L Brandi, W. W De Herder, G. Kaltsas, P. Komminoth, J-Y Scoazec, R. Salazar, A. Sauvanet, R. Kianmanesh, et al. "ENETS Consensus Guidelines for the management of patients with liver and other distant metastases from neuroendocrine neoplasms of foregut, midgut, hindgut, and unknown primary". In: *Neuroendocrinology* 95.2 (2012), pp. 98–119.

[38] BLR Kam, JJM Teunissen, EP Krenning, WW De Herder, Saima Khan, EI Van Vliet, and Dirk Jan Kwekkeboom. "Lutetium-labelled peptides for therapy of neuroendocrine tumours". In: *European journal of nuclear medicine and molecular imaging* 39.1 (2012), pp. 103–112.

[39] Steven M Larson, Andrew Raubitschek, James C Reynolds, Ronald D Neumann, Karl-Erik Hellstrom, Ingegerd Hellstrom, David Colcher, Jeffrey Schlom, Eli Glatstein, and Jorge A Carrasquillo. "Comparison of bone marrow dosimetry and toxic effect of high dose 131 I-labeled monoclonal antibodies administered to man". In: *International Journal of*

Radiation Applications and Instrumentation. Part B. Nuclear Medicine and Biology 16.2 (1989), pp. 153–158.

[40] M. Larsson, P. Bernhardt, J. B. Svensson, B. Wangberg, H. Ahlman, and E. Forssell-Aronsson. "Estimation of absorbed dose to the kidneys in patients after treatment with 177Lu-octreotate: comparison between methods based on planar scintigraphy". In: *EJNMMI Res* 2.1 (2012), p. 49.

[41] R. Loevinger and M. Berman. "A formalism for calculation of absorbed dose from radionuclides". In: *Physics in medicine and biology* 13.2 (1968), pp. 205–17.

[42] R. Lozano, M. Naghavi, K. Foreman, S. Lim, Ke. Shibuya, V. Aboyans, J. Abraham, T. Adair, R. Aggarwal, S. Y Ahn, et al. "Global and regional mortality from 235 causes of death for 20 age groups in 1990 and 2010: a systematic analysis for the Global Burden of Disease Study 2010". In: *The Lancet* 380.9859 (2012), pp. 2095–128.

[43] H. B Mann and D. R Whitney. "On a test of whether one of two random variables is stochastically larger than the other". In: *The annals of mathematical statistics* (1947), pp. 50–60.

[44] *NIST Database for Physical Reference Data.* URL: http://www.nist.gov/pml/data/index.cfm.

[45] Y. C. Patel. "Somatostatin and its receptor family". In: *Frontiers in neuroendocrinology* 20.3 (1999), pp. 157–198.

[46] B. J Pichler, A. Kolb, T. Nägele, and H. Schlemmer. "PET/MRI: paving the way for the next generation of clinical multimodality imaging applications". In: *Journal of Nuclear Medicine* 51.3 (2010), pp. 333–336.

[47] M. Quarantelli and A. Prinster. "Habib Zaidi: Quantitative Analysis in Nuclear Medicine Imaging". In: *European Journal of Nuclear Medicine and Molecular Imaging* 34.10 (2007), pp. 1708–1708.

[48] J. Radon. "1.1 über die bestimmung von funktionen durch ihre integralwerte längs gewisser mannigfaltigkeiten". In: *Classic papers in modern diagnostic radiology* 5 (2005).

[49] JC Sanders, T Kuwert, J Hornegger, and P Ritt. "Quantitative SPECT/CT Imaging of 177Lu with In Vivo Validation in Patients Undergoing Peptide Receptor Radionuclide Therapy". In: *Molecular Imaging and Biology* (2014), pp. 1–9.

[50] M. Sandström, U. Garske-Román, D. Granberg, S. Johansson, C. Widström, B. Eriksson, A. Sundin, H. Lundqvist, and M. Lubberink. "Individualized dosimetry of kidney and bone marrow in patients undergoing 177Lu-DOTA-octreotate treatment". In: *Journal of Nuclear Medicine* 54.1 (2013), pp. 33–41.

[51] W. Schneider, T. Bortfeld, and W. Schlegel. "Correlation between CT numbers and tissue parameters needed for Monte Carlo simulations of clinical dose distributions". In: *Physics in medicine and biology* 45.2 (2000), p. 459.

[52] G. Sgouros. "Bone marrow dosimetry for radioimmunotherapy: theoretical considerations". In: *Journal of Nuclear Medicine* 34.4 (1993), pp. 689–94.

[53] L. A Shepp and Y. Vardi. "Maximum likelihood reconstruction for emission tomography". In: *Medical Imaging, IEEE Transactions on* 1.2 (1982), pp. 113–122.

[54] JA Siegel, BW Wessels, EE Watson, MG Stabin, HM Vriesendorp, EW Bradley, CC Badger, AB Brill, and CS Kwok. "Bone marrow dosimetry and toxicity for radioimmunotherapy." In: *Antibody Immunoconjugates and Radiopharmaceuticals* 3.4 (1990), pp. 213–234.

[55] W. S Snyder, M. R Ford, and G. G Warner. "MIRD pamphlet no. 5, revised: Estimates of specific absorbed fractions for photon sources uniformly distributed in various organs of a heterogeneous phantom". In: *New York, NY: Society of Nuclear Medicine* (1978).

[56] M. Soret, S. L Bacharach, and I. Buvat. "Partial-volume effect in PET tumor imaging". In: *Journal of Nuclear Medicine* 48.6 (2007), pp. 932–945.

[57] C. Spearman. "The proof and measurement of association between two things". In: *The American journal of psychology* 15.1 (1904), pp. 72–101.

[58] M. G. Stabin and J. A. Siegel. "Physical models and dose factors for use in internal dose assessment". In: *Health physics* 85.3 (2003), pp. 294–310.

[59] M. Stabin, J. Siegel, J. Hunt, A. Brill, R. Sparks, K. Eckerman, and L. Bertelli. *RADAR: The RAdiation Dose Assessment Resource*. URL: http://www.doseinfo-radar.com/.

[60] S. Surti, A. Kuhn, M. E Werner, A. E Perkins, J. Kolthammer, and J. S Karp. "Performance of Philips Gemini TF PET/CT scanner with special consideration for its time-of-flight imaging capabilities". In: *Journal of Nuclear Medicine* 48.3 (2007), pp. 471–480.

[61] S. Walrand, M. Hesse, G. Demonceau, S. Pauwels, and F. Jamar. "Yttrium-90-labeled microsphere tracking during liver selective internal radiotherapy by bremsstrahlung pinhole SPECT: feasibility study and evaluation in an abdominal phantom". In: *EJNMMI Res* 1.1 (2011), pp. 1–14.

[62] L. E Williams, A. Liu, D. M Yamauchi, G. Lopatin, A. A Raubitschek, and J. YC Wong. "The two types of correction of absorbed dose estimates for internal emitters". In: *Cancer* 94.S4 (2002), pp. 1231–1234.

[63] K. Willowson, D. L Bailey, and C. Baldock. "Quantitative SPECT reconstruction using CT-derived corrections". In: *Physics in medicine and biology* 53.12 (2008), p. 3099.

[64] J. J Zaknun, L. Bodei, J Mueller-Brand, ME Pavel, RP Baum, D Hörsch, MS ODorisio, TM ODorisiol, JR Howe, M Cremonesi, et al. "The joint IAEA, EANM, and SNMMI practical guidance on peptide receptor radionuclide therapy (PRRNT) in neuroendocrine tumours". In: *European journal of nuclear medicine and molecular imaging* 40.5 (2013), pp. 800–816.

Chapter 5

Original publications

This section contains the original publications which were basis for this cumulative thesis:

A. Delker, H. Ilhan, C. Zach, J. Brosch, F-J. Gildehaus, S. Lehner, P. Bartenstein, and G. Böning. "The Influence of Early Measurements Onto the Estimated Kidney Dose in [177Lu][DOTA0, Tyr3] Octreotate Peptide Receptor Radiotherapy of Neuroendocrine Tumors". In: Molecular Imaging and Biology 17 (5 2015), pp. 726-734.

A. Delker, W. P. Fendler, C. Kratochwil, A. Brunegraf, A. Gosewisch, F-J. Gildehaus, S. Tritschler, C. G. Stief, K. Kopka, U. Haberkorn, P. Bartenstein, and G. Böning. "Dosimetry for Lu-177-DKFZ-PSMA-617: a new radiopharmaceutical for the treatment of metastatic prostate cancer". In: European journal of nuclear medicine and molecular imaging 43 (1 2015), pp. 42-51.

RESEARCH ARTICLE

The Influence of Early Measurements Onto the Estimated Kidney Dose in [^{177}Lu][DOTA^0,Tyr^3] Octreotate Peptide Receptor Radiotherapy of Neuroendocrine Tumors

Andreas Delker, Harun Ilhan, Christian Zach, Julia Brosch, Franz Josef Gildehaus, Sebastian Lehner, Peter Bartenstein, Guido Böning

Department of Nuclear Medicine, University Hospital, Ludwig-Maximilians-Universität, Munich, Germany

Abstract

Purpose: Multiple measurements have been required to estimate the radiation dose to the kidneys resulting from [^{177}Lu]DOTATATE therapy for neuroendocrine tumors. The aim of this study was to investigate the influence of early time-point measurement in the renal dose calculation.

Procedures: Anterior/posterior whole-body planar scintigraphy images were acquired at approx. 1, 24, 48, and 72 h after administration of [^{177}Lu]DOTATATE. Furthermore, we acquired planar 1-bed dynamic recordings in 12 frames (5 min each) during the first hour. We assessed kidney exposure with a three-phase model consisting of a linear increase to the maximum within the initial minutes p.i., followed a bi-exponential decline. This three-phase-model served as reference for evaluating accuracy of dose estimates in 105 kidneys calculated by conventional mono-exponential fitting of the final three and four whole-body images.

Results: Mean effective half-life times for the reference model were 25.8±12.0 min and 63.9±17.6 h, predicting a mean renal dose of 5.7±2.1 Gy. The effective half-life time was 46.3±15.4 h for the last four and 63.3±17.0 h for the last three data points. The mean start of the first whole-body measurement was 1.2±0.1 h p.i. The ratio of fast to slow phases was 28.1±23.9 % at this time point, which caused a mean absolute percentage dose deviation of 12.4 % for four data points, compared to 3.1 % for three data points. At a mean time of 2.4 h p.i. (max 5.1 h), the ratio of fast to slow phase declined below 5 %.

Conclusions: Kinetic analysis of renal uptake using dynamic planar scans from the first hour after injection revealed a fast and a slow washout phase. Although the fast phase did not contribute substantially to the estimated renal dose, it could influence planar measurements performed within the first hours. We found that the presence of two clearance phases can hamper accurate dose estimation based on a single-phase model, resulting in approximately 12.4 % dose underestimation, thus potentially resulting in overtreatment. In the absence of dynamic initial recordings, the first dosimetry measurements should therefore be obtained later than 3–5 h after [^{177}Lu]DOTATATE injection. Omitting the early whole-body image reduced the dose estimation error to 3.1 %.

Key words: Neuroendocrine tumor, Lutetium 177, Kidney dose, Dosimetry, Peptide receptor radionuclide therapy

Correspondence to: Guido Böning; *e-mail:* guido.boening@med.uni-muenchen.de

Introduction and Aim

Peptide receptor radionuclide therapy (PRRT) with radiolabeled somatostatin analogues has emerged as a well-established therapy option in the management of patients with metastasized neuroendocrine tumors (NETs) expressing somatostatin receptors, according to recently established guidelines [1, 2]. Currently, the most commonly used compounds are $[^{90}Y][DOTA^0,Tyr^3]$octreotide ($[^{90}Y]$DOTATOC) and $[^{177}Lu][DOTA^0,Tyr^3]$octreotate ($[^{177}Lu]$ DOTATATE). Response to therapy is encouraging, with progression free survival of 33 months and overall survival rates up to 46 months [3, 4]. Although PRRT is well tolerated in most NET patients, and severe complications are rare, radiation toxicity remains a therapy-limiting factor. Whereas hematoxicity is fortunately reversible in most cases, the kidneys are particularly at risk for overexposure [5, 6]. Cumulative dose values ranging from 23 to 29 Gy to the kidneys are reported as acceptable, in the absence of additional renal risk factors [7, 8].

PRRT with the beta- and gamma-emitting somatostatin analogue $[^{177}Lu]$DOTATATE is accompanied with fewer side effects and yet equally successful therapy response rates as compared to $[^{90}Y]$DOTATOC [3]. Furthermore, Lu-177 lends itself better for performing image-based dosimetric studies because of the gamma component, which allows simultaneous scintigraphy marking the beta treatment. Therapy is usually performed with standard doses of 7.4 GBq per cycle within four to six cycles [2]. Dose escalation and optimal patient-specific treatment informed by pre- and peri-therapeutic dosimetry findings, however, might enable maximal radiation dose to the tumors.

In general, the radiation exposures of the tumor and also the risk organs have to be monitored at intervals during the therapy so that total doses in the regions of interest can be calculated with some accuracy. A few well-selected time points must serve to this end, sparing the expense and effort entailed in collecting a prolonged series of measurements. In this regard, Larsson et al. [9] emphasized the importance of late time points for estimating radiation dose due to the long physical half-life of Lu-177. We now aim of optimizing clinical dosimetry with consideration of the influence of early time points on the estimation of kidney dose using a multi-phase kinetic model.

Material and Methods

Patients and Therapy

Patients with histologically proven well-differentiated metastatic NETs with expression of somatostatin receptors and a Ki-67 proliferation marker under 20 % were treated in multiple cycles with a default activity of 7.4 GBq $[^{177}Lu]$DOTATATE per cycle. Labelling of the precursor DOTATATE (ABX GmbH, Radeberg, Germany) was performed according to the method described by Breeman et al. [10] with slight modifications. The labelling with n.c.a. Lu-177 (ITG GmbH, Garching, Germany) was performed with 125 μg peptide precursor in acetate buffer (pH 4.7). The radiochemical yield was greater than 95 % and the radiochemical purity greater than 98 % in the final preparation. For kidney dose estimation of one treatment cycle, we collected a sample of 64 (27 female, 37 male) consecutive patients (aged 62±12 years; range 22–89 years). In some cases, more than one therapy cycle was used for the data analysis, resulting in a total of 105 datasets. The radiopharmaceutical was intravenously infused during 30 min at a rate of 1.6 ml/min. For prophylaxis against kidney damage, the i.v. administration of 1 l of an arginine and lysine solution (Pharmacy of the University Hospital of Munich, Germany) was initiated 30 min prior to the administration of the therapeutic (rate 5.8 ml/min).

Acquisition

Prior to therapy, a diagnostic PET/CT scan (Biograph 64 TruePoint, Siemens Medical Solutions) using $[^{68}Ga]$DOTATATE had been performed to locate the tumor metastasis and to quantify the maximum standardized uptake value (SUVmax) of the tumor lesion.

For therapy monitoring and dosimetry estimation, distribution of the therapeutic agent $[^{177}Lu]$DOTATATE was assessed dynamically with a dual-headed scintillation camera (E.cam, Siemens Medical Solution, 16 mm NaI(Tl) crystal) equipped with medium energy parallel hole collimators. Patients were positioned on the camera table in supine feet-first orientation. Detector heads were positioned in the anterior and posterior locations. An energy window was centered on the major gamma photon peak of the Lu-177 decay series (208 keV, width=15 %), together with additional windows (240 keV, width=10 %; 170 keV, width=15 %) to allow for scatter correction using the triple energy window method. Upon beginning the $[^{177}Lu]$DOATATE infusion, a dynamic sequence of 12 planar frames (of 5 min each) was initiated in a 128×128 matrix of 4.8 mm pixels. Thereafter, whole-body images were acquired over 20 min in a 1024×256 matrix of 2.4 mm pixels at approximately 1, 24, 48, and 72 h post injection (or day 0, 1, 2, and 3 p.i.). An example series of posterior images is shown in Fig. 1.

The patient's urine was collected from a bladder catheter (female patients) or urine bottle (male patients) from the start of the infusion until the start of the first whole-body scan at approximately 1 h post injection to determine the net activity in the early images. For that purpose, the activity of 1-ml portions of the urine samples was measured with a high purity semi-conductor Germanium detector (Canberra Industries Inc. Model Gr0820) from which the total activity of the entire collected volume was calculated.

Planar Quantification

Scatter correction was performed according to the triple energy window method described by Ichihara et al. [11]. For attenuation correction, the patient thickness and the kidney thickness were measured from the CT image, which had been obtained during diagnostic imaging. Furthermore, the kidney mass was determined for later dose calculations.

The activity A_j in a source region j was calculated according to Eq. 1. Attenuation correction was therein performed according to

Fig. 1 Posterior planar whole-body view approx. 1, 24, 48, and 72 h (from *left* to *right*) after administration of [^{177}Lu]DOTATATE.

the method published by Fleming *et al.* [12] and as suggested in the MIRD 16 Pamphlet [13] for isolated single source regions, with a correction for the source region attenuation f_j and the source thickness x_j with the coefficient μ_j.

$$A_j = \sqrt{\frac{I_A I_P}{e^{-\mu_e x}}} \, \frac{\left(\mu_j x_j/2\right)}{C \sinh\left(\mu_j x_j/2\right)} = \sqrt{\frac{I_A I_P}{e^{-\mu_e x}}} \, \frac{f_j}{C} \qquad (1)$$

where I_A and I_P are the counts per second (cps) detected in the anterior and posterior region of interest (ROI) j. The exponential term $e^{-\mu_e x}$ represents the transmission factor for a patient with the total thickness x (cm) and with an individual attenuation value μ_e. For the attenuation coefficients, we used the four component soft tissue values obtained from the XCOM cross section database [14]. C is the calibration factor for each individual patient and therapy cycle in cps/Bq determined from the sum of counts in the first whole-body planar image, divided by the net remaining activity in this image.

To calculate the kidney counts, ROIs were drawn around the organ boundaries to scintigraphy, and attenuation corrected as described above. For background correction, an ROI was placed in an area without specific tracer accumulation, such as the lower abdomen or the thigh and subtracted with the method described by Kojima *et al.* [15] and presented in the MIRD 16 Pamphlet as "Background Subtraction: A Single Well-Defined Source Region Surrounded by Regions of Background Activity" to avoid over subtraction of background activity. Finally, the sum of counts from a whole-body ROI at day 0 were divided by the total administered activity, less the activity lost to micturition (1.3±0.5 GBq, range 0.1–2.2 GBq). Only those organs without allocation of extra activity uptake due to overlay effects were analyzed; the right kidney was overlapped by liver activity in many projection images. Therefore, we decided to investigate solely the effect of early measurement time points for the left kidney. Patient data was excluded from this study when overlay of extrarenal activity was present in the images of the left kidney.

Dose Calculations

The dose calculations in this work were performed according to the MIRD scheme [16]. The radiation dose is assessed by describing activity in source regions which irradiate target regions, as well as self-radiation of the target. The dose to a given target area is then calculated as the sum of all dose fractions from the source regions. To simplify the calculation, we assumed that most of the radiation damage to organs is caused by the beta radiation of Lu-177 and therefore neglected the irradiation by gamma-photons arising from other source regions. The mean absorbed dose D to the kidney was then calculated by:

$$D = \widetilde{A} \times S \qquad (2)$$

$\widetilde{A}$ is the accumulated activity in the kidney (as a measure of all nuclear transitions) and S is the mean absorbed dose per unit accumulated activity (or the mean absorbed dose per nuclear transition). We applied a three-phase model (TrBi-exp) consisting of a linear increase to the maximum within the initial minutes of the infusion and a bi-exponential decline describing a rapid distribution phase and a slow washout/elimination phase. The bi-exponential function was fitted using the nonlinear least squares method in MATLAB (R2011a, The MathWorks, Inc.). To obtain the sum of all nuclear transitions, this three-phase model was integrated over time to infinity. The cumulated activity $\widetilde{A}$ was then used to estimate the absorbed dose D together with the kidney-specific S value for Lu-177 obtained from the RADAR website [17]. A rescaling to the individual patient kidney mass was performed according to [18]

$$S(\text{patient}) = S(\text{MIRD}) \frac{m(\text{MIRD})}{m(\text{patient})} \qquad (3)$$

using the MIRD mass and *S* values from the kidneys of the adult phantoms [19].

Investigating the Effect of Early Time Points

The integrated activity of TrBi-exp served as baseline for evaluating kidney doses calculated from four whole-body static images at approx. 1, 24, 48, and 72 h p.i. (4P-fit) or only the last three whole-body images (3P-fit). We compared a mono-exponential function with two parameters

$$f_0(t) = p_1 e^{-p_2 t} \qquad (4)$$

as the null hypothesis, with a set of three-parametrical fit functions as the alternate hypothesis, with fit parameters p_i and—in the case of Eq. 5b as in [20, 21]—with a separate consideration of the physical decay constant λ_{phys}

$$f_1(t) = p_1 \left(e^{(-p_2 t)} + e^{(-p_3 t)} \right) \qquad (5a)$$

$$f_2(t) = p_1 e^{-(p_2 + \lambda_{phys})t} + p_3 e^{-\lambda_{phys} t} \qquad (5b)$$

The most appropriate model f_m (with m being 0, 1, or 2, as defined in equations 4 and 5) was then chosen by performing the F test [20]. For the null hypothesis (null) and the alternative hypothesis (alt), the squares of the residuals between fitted model and measured data points were summed yielding SSR_{null} and SSR_{alt}. The corresponding degrees of freedom, DF_{null} and DF_{alt}, were calculated by subtracting the number of fit parameters from the number of available measurement points. The F value was then obtained by:

$$F = \frac{(SSR_{null} - SSR_{alt})\, DF_{alt}}{(DF_{null} - DF_{alt})\, SSR_{alt}} \qquad (6)$$

If the p value was under the significance level of $\alpha = 0.05$, the null hypotheses was rejected, and the alternate model was used. The corrected Akaike Information Criterion (AICc), which is proposed by Glatting et al. [20] and Kletting et al. [22], is not here feasible, since AICc requires at least three more data points than the number of parameters. For the case of the 3P-fit, we used the mono-exponential function (Eq. 4) with two parameters to increase the probability for successful fitting of noisy data by providing a model which has fewer fit parameters than the number of available data points. Using the model f_m which was selected by the F test for each individual patient j, we then determined the percentage deviation of the accumulated activity $\widetilde{A}_{m,j}$ relative to the accumulated activity $\widetilde{A}_{TrBi,j}$ of the baseline model TrBi-exp:

$$\%DEV_j = \frac{\widetilde{A}_{m,j} - \widetilde{A}_{TrBi,j}}{\widetilde{A}_{TrBi,j}} \times 100 \qquad (7)$$

Thus, a negative %DEV would indicate underestimation and a positive %DEV overestimation of the real dose. We calculated the corresponding mean deviation from baseline for all n patients using the appropriate model f_m for each patient j as selected by the F test:

$$M = \frac{1}{n} \sum_{j=1}^{n} |\%DEV_j| = \frac{1}{n} \sum_{j=1}^{n} \left| \frac{\widetilde{A}_{m,j} - \widetilde{A}_{TrBi,j}}{\widetilde{A}_{TrBi,j}} \right| \times 100 \qquad (8)$$

Results

Calculated Dose with TrBi-exp

All bi-exponential curve fits succeeded, with a mean coefficient of determination (R^2) value of 0.995±0.010 and minimum R^2 of 0.973. Data for a representative kidney time activity curve is shown in Fig. 2, with the bi-exponential fit in green. This bi-exponential consists of two phases, which can interfere during the first hours. The population mean effective half live $T_{1/2}$ was 25.8±12.0 min for the fast phase and 63.9±17.6 h for the slow phase. Using the TrBi-exp model, the mean calculated dose of all 105 patient datasets was 5.7±2.1 Gy (range 2.5–13.8 Gy), which gave a mean kidney dose of 0.8±0.3 Gy/GBq administered. Because TrBi-exp is a linear combination of three functions, the mean dose factors and the percentage contribution to the total dose can be specified separately (Table 1). The kidney masses used for mass correction of the S values according to Eq. 3 ranged from 104 to 396 g, with a mean value of 186±45 g.

Dosimetry Using Four Whole-Body Planar Image Time Points (4P-fit)

Before calculating the accumulated activity from only four late scintigraphy measurements, the best fitting of a set of models was chosen with the F test, as described above. In five of 105 cases, the model f_1 (Eq. 5a) was favored instead of the mono-exponential function, for which an example is shown in Fig. 3a. In this graph, the bi-exponential part of the baseline function (green), mono-exponential (cyan) and $f_1(t)$ (purple) functions are visualized. In most cases, the alternative models were rejected, as illustrated in Fig. 3b, where the baseline (green) and the mono-exponential (cyan) fits are plotted together with the fits onto model $f_1(t)$ (purple). Using the matching fit model for each kidney the mean R^2 was 0.965±0.032 for the 4P-fit. Analyzing the fit parameters indicated an initial mean activity from parameter p_1 in the kidneys of 153.8±56.1 MBq (range 71–389 MBq). For the slow washout parameter, the mean half-life for 4P-fit was 46.3±15.4 h (range 21.5–90.5 h). The calculated dose with these parameters was 5.0±1.9 Gy (range 2.5–11.3 Gy).

Dosimetry Using 3 Whole-Body Planar Image Time Points (3P-fit)

Omitting the first measurement point at approx. 1 h p.i. and using the mono-exponential fit (3P-fit), the mean R^2 was 0.983±0.030. Analysis of the fit parameters indicated a mean initial activity of 126.5±39.2 MBq (range 45–258 MBq) in the kidneys and a mean effective half-life of 63.3±17.0 h (range 34.1–115.1 h). The resulting mean dose was 5.6±2.1 Gy (range 2.5–14.1 Gy).
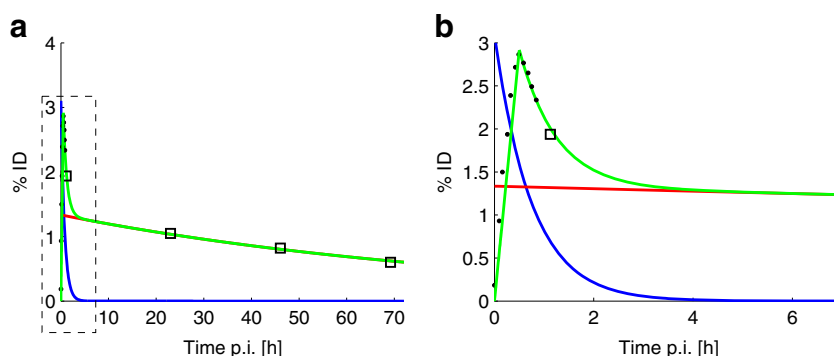
Fig. 2 a Time activity curve of the left kidney of a patient with dynamic planar measurement of $[^{177}Lu]$DOTATATE within the first hour (*filled circles*) and planar whole body scintigraphies up to 70 h post injection (*open squares*). The bi-exponential fit is plotted in green and its two exponentials, which represent the different phase fractions, are plotted in *blue* (fast; $T_{1/2}$=31 min) and *red* (slow; $T_{1/2}$=63 h). **b** This plot focuses on the early phase within the first 6 h indicated by the *dashed rectangular area* in (**a**) so as to visualize the linear increase to the maximum within the initial minutes of the infusion.

Comparison of Dose Estimation Approaches with Baseline

The deviation of the dose calculated with 3P-fit (blue) and 4P-fit (red) from the dose calculated with TrBi-exp is presented for each of the 105 kidneys in Fig. 4a. In only 7 of 105 datasets was the absolute deviation from the calculated dose higher when the first measurement point was omitted. We saw a maximum absolute deviation of 41.1 % with the 4P-fit compared to a maximum of 13.8 % with 3P-fit, calculated relative to the baseline method. The mean absolute percentage deviation was 12.4±9.2 % with four points and 3.1±2.5 % with three points. With the exception of six patients, the calculated dose with four points was always underestimated, whereas the calculation with three time points underestimated dose in 65 and overestimated in 40 cases. Calculated doses of the baseline model TrBi-exp, 4P-fit, and 3P-fit are shown in Fig. 4b. The mean dose value with four late points was significantly decreased compared to the other two methods.

Discussion

Considering the generally impaired health status of most patients undergoing PRRT, it is mandatory to obtain reliable dosimetric data with a minimal number of measurements. As in previous dosimetry investigations [23–25], we decided to conclude dosimetry monitoring at 72 h because of logistic reasons. This work is based on the assumption that all kinetic models are valid beyond the last data point at 72 h p.i. Although we have no proof that this assumption holds,

others who had measurements available over a longer time interval, *e.g.*, until approximately 168 h [9, 26, 27], have not observed a deviation of data and exponential model at later times. We therefore assume that the models utilized in this work are suitable descriptions for estimation of the kidney dose. The contribution of the first 72 h to the kidney dose calculated using our proposed reference model TrBi-exp was approximately 54.6±9.2 % (range 34.1–73.7 %).

The limitation to planar scintigraphies is a potential weakness of this study since quantitation of planar scintigraphy is subject to several caveats arising from attenuation and overlap of tissues. Especially, uncertainties due to overlap could be prevented, and radionuclide concentration calculations could be improved by performing 3D dosimetry based on quantitative SPECT/CT measurements [27]. Recent SPECT/CT studies utilizing the radionuclide Lu-177 reported encouraging accuracies and methods in quantitative imaging [28, 29]. The patient group in this study was preselected to contain no obvious kidney overlay in the planar images; therefore, we did not expect a major influence of superpositioned organs. Dosimetry from SPECT/CT images will be addressed in future investigations.

In this paper, we studied the effect of reducing the number of time samples on the outcome of the dosimetry calculations, based on various kinetic models and truncation of the data to as few as three time points. Present data show that the concentration of radioactivity derived from $[^{177}Lu]$DOTATATE in the kidneys is not well described using a single exponential function; we tested several simple multi-phase models, the best of which proved to be a model composed of three phases. Here, the fast initial uptake phase

Table 1. Absolute and relative contribution of the single phases to the total dose function TrBi-exp. Each value was obtained from 105 kidneys

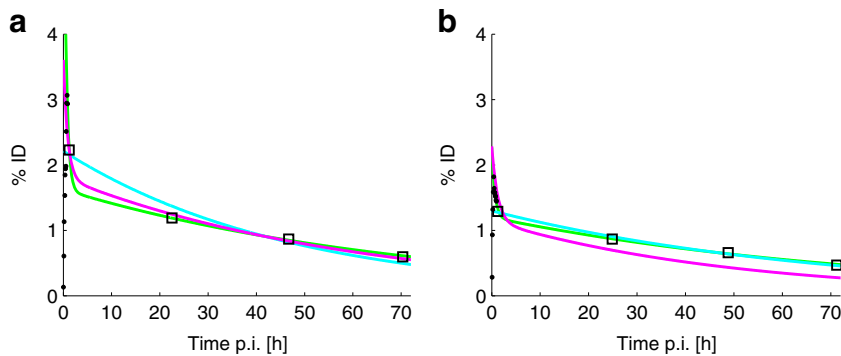| Function	Mean [Gy]	SD [Gy]	Min. [Gy]	Max. [Gy]	Rel. [%]
Linear phase	0.03	0.01	0.01	0.08	0.6
Fast phase	0.03	0.03	0.003	0.19	0.6
Slow phase	5.6	2.1	2.5	13.8	98.9
TrBi-exp (all)	5.7	2.1	2.5	13.8	100

Fig. 3 Example of fit models with four static planar kidney measurement points. **a** The mono-exponential fit is plotted in cyan (R^2=0.968) and function $f_1(t)$ (Eq. 5a) is plotted in purple (R^2=0.997). The F test indicated $f_1(t)$ to be superior in this case ($P<0.025$). For comparison, TrBi-exp is plotted in *green*. **b** A representative patient in whom the F test rejected $f_1(t)$. Here, the mono-exponential fit (cyan; R^2=0.994) was superior to the model $f_1(t)$ (Eq. 5a, R^2=0.541).

was described by a linear increase from time 0 to the time of maximum tracer concentration in the kidneys and was followed by a linear combination of two exponential functions, representing phases of elimination with different time characteristics. For the group of patients, this model gave mean effective half-lives of 25.8±12.0 min for the fast phase and 63.9±17.6 h for the slow phase. In pharmacokinetic studies, such results are generally interpreted to reveal a distribution phase followed by a slow elimination phase. Comparing the mean relative contributions to the total absorbed dose (Table 1), we found that almost the entire dose (98.9 %) is attributable to the slow phase component. The mean dose values for the left kidney per therapy cycle were 5.7±2.1 Gy (0.8±0.3 Gy/GBq), which is in good accordance to previous studies [26, 30, 31]. In agreement with Sandstroem *et al.* [27] and others [32], we noticed a wide range of kidney doses (2.5–13.8 Gy; median 5.3 Gy), likely reflecting a wide range of renal absorption and elimination parameters of the multi-phase kidney activity kinetics in this heterogeneous population. The occurrence of this observed dose variation, where individuals at the high end might easily encounter radiotoxicity, substantiates the need for an individualization of the peptide radionuclide receptor therapy.

A systematic analysis of the observed multi-phase model yielded the following results; based on earlier reports [13, 27], we at first expected an overall higher dose if the first data point was measured during the fast elimination phase. Comparing the mean initial activities in the kidney from 4P-fit (153.8±56.1 MBq) and 3P-fit (126.5±39.2 MBq), indicated a 21.3 % higher calculated dose, as expected for the 4P-fit. Comparing the time activity curve of one representative patient's dataset (Fig. 5) indicated a considerable overestimation of initial uptake, propagating to an artifact of increased area under the curve within the first days after treatment. However, we also observed a steeper descent of the exponential curve caused by the elevated first data point, which led to systematic underestimation of the half-life of the exponential. Hence, when integrating these exponentials to infinity, the area under the entire curve (*i.e.*, the total dose) would consequently be substantially smaller than as predicted by the baseline or the 3P-fit models. Consequent underestimation of the total calculated dose is illustrated by comparison of Fig. 4.

This finding is in concordance with the earlier observations of Guerriero *et al.* [23], who also investigated the accuracy of estimated dose when certain data points were omitted. Their remarks on the inadequate number of
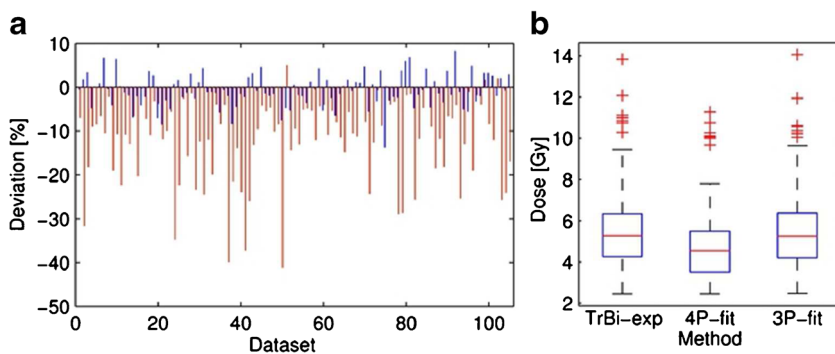

Fig. 4 **a** Comparison of the percentage deviation to TrBi-exp with all four planar measurement time points (4P-fit; *red*) or only the last three planar measurement points (3P-fit; *blue*) of all 105 patient datasets. A *positive value* indicates an overestimation and a *negative value* an underestimation of the dose. **b** *Boxplots* of the dose calculated with TrBi-exp (*left*), 4P-fit (*middle*), and 3P-fit (*right*). Outliers are plotted individually (*red*).

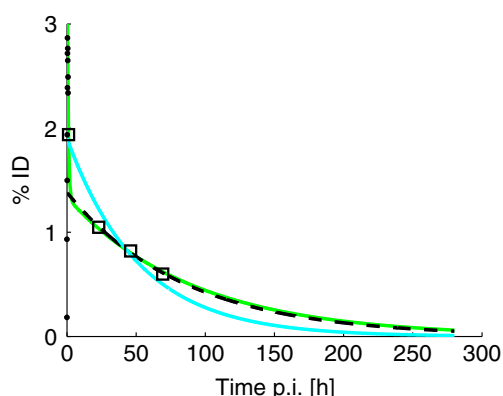**Fig. 5** Comparison of fits of planar scintigraphy data with four points (4P-fit, *cyan*), 3 points (3P-fit, *dashed black*), and the bi-exponential fit (Bi-exp, *green*) including the dynamic data during the first 30 min after infusion. The *abscissa* is extended to distinguish the gradients of the curves.

Fig. 6 Percentage dose deviation compared to the baseline function TrBi-exp with four time points (*red*) and the last three time-points (*blue*) as functions of the ratio of fast to slow phases at the first whole-body measurement day. A linear regression is shown for both cases.

available data points to describe multiple phases arose from SPECT images at comparable time points as in the present work, except that no dynamic sampling of the initial fast phase was available to them. Provided with the initial dynamic data, we concur with their observations. Furthermore, our data allow us to describe the fast and slow phases separately and predict a time point after which the influence of the fast phase onto the overall time activity curve diminishes. In contrast to [9], where kidney dose was assessed by four planar images during days 0, 1, 2, and 7, we did not observe peak activities in the kidneys at day 1 or later. Omitting the late day 7, data point had a noticeable effect on the estimated kidney dose in their work. As this situation is similar to using the 4P-fit in our present work but with day 2 constituting the latest time point, our findings indicate that this effect may rather be related to the mixture of the fast and slow retention phases in the early data points, but in concordance with [9], the effect could be weakened when data points later than day 3 are included.

To study the fast-phase influence on the day 0 whole-body image in some detail, we calculated the ratio between fast and slow phases from the bi-exponential model. The mean time of the first whole-body measurement was 1.2 ±0.1 h after injection, when the mean relative ratio between the fast and slow phases was 28.1±23.9 %. The mean time point at which this ratio fell below an arbitrary value of 5 % was 2.4 h p.i. (max 5.1 h), whereupon the contribution of the first phase might safely be ignored. Figure 6 illustrates the effect on treatment day 0 of this influenced measurement onto the percentage dose deviation (compared to TrBi-exp), when the total dose was calculated with (4P-fit, red) or without (3P-fit, blue) the day 0 measurement. The Spearman's test gave ρ of 0.91 (4P-fit), indicating a very strong correlation between the dose deviation and the contribution of the fast retention phase to the day 0 measurement. In the case of the three time points (3P-fit), no such correlation was found (ρ=0.01).
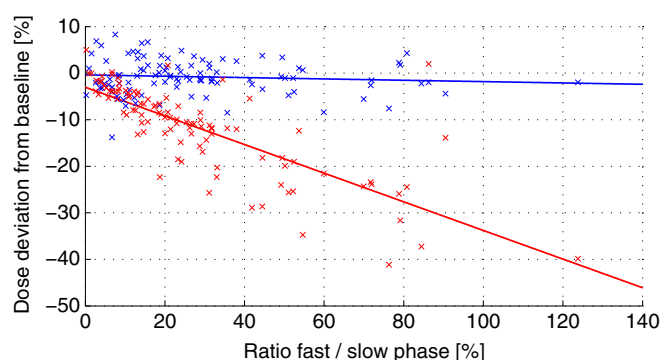
The coefficient of determination R^2 of the 4P-fit was consistently high (circa 0.97), which would not in itself alert to this bias. Nevertheless, the utilization of more sophisticated fitting algorithms, which assign individual weights to each measurement point, is certainly sufficient to reduce the mismatch between treatment day measurements and the chosen mono-exponential kinetic model. Our observations confirm that high R^2 values cannot be relied upon as proof of model fitness but that curve fits should be carefully checked by an experienced reader. This is illustrated in Fig. 5, where the 4P-fit results in R^2 of 0.95, although this fit clearly does not represent the true situation. The inadequacy of R^2 as an indicator for the fit quality of nonlinear functions is in accordance with Spiess *et al.* [33]. When the same model is applied to only a subgroup of these data, *i.e.*, omitting the treatment day whole-body scan, the accuracy of the results could be significantly improved. Nevertheless, limitations could arise from this reduction of data especially if one of the remaining measurements is not available due to a hardware failure or patient discomfort. It is generally understood that at least three data points are needed for modelling an exponential phase, as noted by Lassmann *et al.* [34].

A mean dose deviation from the 4P-fit of 12.4±9.2 % in a single therapy cycle is unlikely to be a factor in the risk for radiation-induced nephropathy. However, an accumulation of such dose underestimations in multiple therapy cycles could well lead to a substantial and relevant underestimation of total radiation dose to the kidneys. In three of 105 individual cases, we observed a dose deviation for the 4P-fit of up to 40 %, corresponding to 3 Gy in a single cycle (see Fig. 4a). In seven of 105 datasets, the underestimation exceeded 2 Gy. If dose estimates from individuals are used for designing dosimetry-supported individualized therapies, the observed underestimations would cause ill-planning of therapeutic doses of subsequent cycles. Hence, the risk of receiving a critically high radiation dose increases significantly for patients across the treatment cycle.

Conclusion and Outlook

We studied the effect of reducing the number of measurement times on the outcome of dosimetry calculations based on various multi-phase descriptions of the kidney activity following a [^{177}Lu]DOTATATE treatment cycle in a series of 64 NET patients. We found that the majority of the kidney dose occurs during the slow washout phase, which is integrated to infinity, as in conventional pharmacokinetic models. We also found that interference of early measurements by the fast washout phase biases the results, sometimes resulting in severe underestimation of the kidney dose. This work demonstrates that the accuracy of dosimetric values for the kidneys largely depends on a proper determination of the slow phase for renal washout. However, careful selection of data points avoids errors arising from integration of unsuitable early data, which may be affected by the fast phase. These observations support reducing the number of scintigraphy measurements without compromising the accuracy of image-based dosimetry. These findings should facilitate optimized dosimetry scanning protocols, while minimizing the work load for staff and patients. Scintigraphy results may generalize to quantitative SPECT measurements, which are not dependent on the whole-body calibration. Thus, we recommend starting the first dosimetric measurement 24 h after radiotherapeutic agent injection.

References

1. Pavel M, Baudin E, Couvelard A et al (2012) ENETS consensus guidelines for the management of patients with liver and other distant metastases from neuroendocrine neoplasms of foregut, midgut, hindgut, and unknown primary. Neuroendocrinology 95:157–176
2. Bodei L, Mueller-Brand J, Baum RP et al (2013) The joint IAEA, EANM, and SNMMI practical guidance on peptide receptor radionuclide therapy (PRRNT) in neuroendocrine tumours. Eur J Nucl Med Mol Imaging 40:800–816
3. van der Zwan WA, Bodei L, Mueller-Brand J, et al. (2014) GEP-NETS update: radionuclide therapy in neuroendocrine tumors. European journal of endocrinology / European Federation of Endocrine Societies
4. Koch W, Auernhammer CJ, Geisler J et al (2014) Treatment with octreotide in patients with well-differentiated neuroendocrine tumors of the ileum: prognostic stratification with Ga-68-DOTA-TATE positron emission tomography. Mol Imaging 13:1–10
5. Bodei L, Cremonesi M, Grana CM et al (2012) Yttrium-labelled peptides for therapy of NET. Eur J Nucl Med Mol Imaging 39(Suppl 1):S93–S102
6. Kam BL, Teunissen JJ, Krenning EP et al (2012) Lutetium-labelled peptides for therapy of neuroendocrine tumours. Eur J Nucl Med Mol Imaging 39(Suppl 1):S103–S112
7. Konijnenberg M, Melis M, Valkema R et al (2007) Radiation dose distribution in human kidneys by octreotides in peptide receptor radionuclide therapy. J Nuclear Med : Off Public Soc Nuclear Med 48:134–142
8. Emami B, Lyman J, Brown A et al (1991) Tolerance of normal tissue to therapeutic irradiation. Int J Radiat Oncol Biol Phys 21:109–122
9. Larsson M, Bernhardt P, Svensson JB et al (2012) Estimation of absorbed dose to the kidneys in patients after treatment with ^{177}Lu-octreotate: comparison between methods based on planar scintigraphy. EJNMMI Res 2:49
10. Breeman WA, De Jong M, Visser TJ et al (2003) Optimising conditions for radiolabelling of DOTA-peptides with ^{90}Y, ^{111}In and ^{177}Lu at high specific activities. Eur J Nucl Med Mol Imaging 30:917–920
11. Ichihara T, Ogawa K, Motomura N et al (1993) Compton scatter compensation using the triple-energy window method for single- and dual-isotope SPECT. J Nuclear Med : Off Public Soc Nuclear Med 34:2216–2221
12. Fleming JS (1979) A technique for the absolute measurement of activity using a gamma camera and computer. Phys Med Biol 24:176–180
13. Siegel JA, Thomas SR, Stubbs JB et al (1999) MIRD pamphlet no. 16: techniques for quantitative radiopharmaceutical biodistribution data acquisition and analysis for use in human radiation dose estimates. J Nuclear Med : Off Public Soc Nuclear Med 40:37S–61S
14. Berger MJ, Hubbell JH, Seltzer SM (2010) XCOM: photon cross section database (version 1.5). http://physics.nist.gov/xcom. National Institute of Standards and Technology, Gaithersburg
15. Kojima A, Takaki Y, Matsumoto M et al (1993) A preliminary phantom study on a proposed model for quantification of renal planar scintigraphy. Med Phys 20:33–37
16. Loevinger R, Berman M (1968) A formalism for calculation of absorbed dose from radionuclides. Phys Med Biol 13:205–217
17. Stabin M, Siegel J, Hunt J et al (2001) RADAR: the radiation dose assessment resource. J Nucl Med 42
18. Williams LE, Liu A, Yamauchi DM et al (2002) The two types of correction of absorbed dose estimates for internal emitters. Cancer 94:1231–1234
19. Stabin MG, Xu XG, Emmons MA et al (2012) RADAR reference adult, pediatric, and pregnant female phantom series for internal and external dosimetry. J Nuclear Med : Off Public Soc Nuclear Med 53:1807–1813
20. Glatting G, Kletting P, Reske SN et al (2007) Choosing the optimal fit function: comparison of the Akaike information criterion and the F-test. Med Phys 34:4285–4292
21. Kletting P, Schimmel S, Kestler HA et al (2013) Molecular radiotherapy: the NUKFIT software for calculating the time-integrated activity coefficient. Med Phys 40:102504
22. Kletting P, Kull T, Reske SN, Glatting G (2009) Comparing time activity curves using the Akaike information criterion. Phys Med Biol 54:N501–N507
23. Guerriero F, Ferrari ME, Botta F et al (2013) Kidney dosimetry in (1)(7)(7)Lu and (9)(0)Y peptide receptor radionuclide therapy: influence of image timing, time-activity integration method, and risk factors. BioMed Res Int 2013:935351
24. Baechler S, Hobbs RF, Prideaux AR et al (2008) Extension of the biological effective dose to the MIRD schema and possible implications in radionuclide therapy dosimetry. Med Phys 35:1123–1134
25. Cremonesi M, Botta F, Di Dia A et al (2010) Dosimetry for treatment with radiolabelled somatostatin analogues. a review. Quart J Nuclear Med Molec Imag : Off Public Italian Assoc Nuclear Med 54:37–51
26. Garkavij M, Nickel M, Sjogreen-Gleisner K et al (2010) 177Lu-[DOTA0, Tyr3] octreotate therapy in patients with disseminated neuroendocrine tumors: analysis of dosimetry with impact on future therapeutic strategy. Cancer 116:1084–1092
27. Sandstrom M, Garske U, Granberg D et al (2010) Individualized dosimetry in patients undergoing therapy with (177)Lu-DOTA-D-Phe (1)-Tyr (3)-octreotate. Eur J Nucl Med Mol Imaging 37:212–225
28. Beauregard JM, Hofman MS, Pereira JM et al (2011) Quantitative (177)Lu SPECT (QSPECT) imaging using a commercially available SPECT/CT system. Cancer Imag : official Public Int Cancer Imag Soc 11:56–66
29. Sanders JC, Kuwert T, Hornegger J, Ritt P (2014) Quantitative SPECT/CT Imaging of Lu with *in vivo* validation in patients undergoing peptide receptor radionuclide therapy. Molec Imag Biol: MIB : Off Public Acad Molec Imag
30. Kwekkeboom DJ, Bakker WH, Kooij PP et al (2001) [^{177}Lu-DOTAOTyr3]octreotate: comparison with [^{111}In-DTPAo]octreotide in patients. Eur J Nucl Med 28:1319–1325

31. Wehrmann C, Senftleben S, Zachert C et al (2007) Results of individual patient dosimetry in peptide receptor radionuclide therapy with ^{177}Lu DOTA-TATE and ^{177}Lu DOTA-NOC. Cancer Biother Radiopharm 22:406–416

32. Helisch A, Forster GJ, Reber H et al (2004) Pre-therapeutic dosimetry and biodistribution of 86Y-DOTA-Phe1-Tyr3-octreotide *versus* 111In-pentetreotide in patients with advanced neuroendocrine tumours. Eur J Nucl Med Mol Imaging 31:1386–1392

33. Spiess AN, Neumeyer N (2010) An evaluation of R2 as an inadequate measure for nonlinear models in pharmacological and biochemical research: a Monte Carlo approach. BMC Pharmacol 10:6

34. Lassmann M, Chiesa C, Flux G et al (2011) EANM dosimetry committee guidance document: good practice of clinical dosimetry reporting. Eur J Nucl Med Mol Imaging 38:192–200

CrossMark

ORIGINAL ARTICLE

Dosimetry for ^{177}Lu-DKFZ-PSMA-617: a new radiopharmaceutical for the treatment of metastatic prostate cancer

Andreas Delker[1] · Wolfgang Peter Fendler[1] · Clemens Kratochwil[2] · Anika Brunegraf[1] ·
Astrid Gosewisch[1] · Franz Josef Gildehaus[1] · Stefan Tritschler[3] · Christian Georg Stief[3] ·
Klaus Kopka[4] · Uwe Haberkorn[2] · Peter Bartenstein[1] · Guido Böning[1]

Abstract

Purpose Dosimetry is critical to achieve the optimal therapeutic effect of radioligand therapy (RLT) with limited side effects. Our aim was to perform image-based absorbed dose calculation for the new PSMA ligand ^{177}Lu-DKFZ-PSMA-617 in support of its use for the treatment of metastatic prostate cancer.

Methods Whole-body planar images and SPECT/CT images of the abdomen were acquired in five patients (mean age 68 years) for during two treatment cycles at approximately 1, 24, 48 and 72 h after administration of 3.6 GBq (range 3.4 to 3.9 GBq) ^{177}Lu-DKFZ-PSMA-617. Quantitative 3D SPECT OSEM reconstruction was performed with corrections for photon scatter, photon attenuation and detector blurring. A camera-specific calibration factor derived from phantom measurements was used for quantitation. Absorbed doses were calculated for various organs from the images using a combination of linear approximation, exponential fit, and target-specific S values, in accordance with the MIRD scheme. Absorbed doses to bone marrow were estimated from planar and SPECT images and with consideration of the blood sampling method according to the EANM guidelines.

Results The average (± SD) absorbed doses per cycle were 2.2±0.6 Gy for the kidneys (0.6 Gy/GBq), 5.1±1.8 Gy for the salivary glands (1.4 Gy/GBq), 0.4±0.2 Gy for the liver (0.1 Gy/GBq), 0.4±0.1 Gy for the spleen (0.1 Gy/GBq), and 44±19 mGy for the bone marrow (0.012 Gy/GBq). The organ absorbed doses did not differ significantly between cycles. The critical absorbed dose reported for the kidneys (23 Gy) was not reached in any patient. At 24 h there was increased uptake in the colon with 50 – 70 % overlap to the kidneys on planar images. Absorbed doses for tumour lesions ranged between 1.2 and 47.5 Gy (13.1 Gy/GBq) per cycle.

Conclusion The salivary glands and kidneys showed high, but not critical, absorbed doses after RLT with ^{177}Lu-DKFZ-PSMA-617. We suggest that ^{177}Lu-DKFZ-PSMA-617 is suitable for radiotherapy, offering tumour-to-kidney ratios comparable to those with RLT agents currently available for the treatment of neuroendocrine tumours. Our dosimetry results suggest that ^{177}Lu-DKFZ-PSMA-617 treatment with higher activities and more cycles is possible without the risk of damaging the kidneys.

✉ Guido Böning
Guido.Boening@med.uni-muenchen.de

1   Department of Nuclear Medicine, Ludwig-Maximilians-University
     of Munich, Marchioninistrasse 15, 81377 Munich, Germany

2   Department for Nuclear Medicine, Heidelberg University Hospital,
     Heidelberg, Germany

3   Department of Urology, Ludwig-Maximilians-University of Munich,
     Munich, Germany

4   Division of Radiopharmaceutical Chemistry, German Cancer
     Research Center (dkfz), Heidelberg, Germany

Introduction

After lung cancer, prostate cancer (PC) is the second most common primary tumour affecting men worldwide. Despite improvements in therapy over the past decades, PC tends to become highly aggressive in most patients over time, ultimately causing the death of more than 250.000 men each year worldwide [1]. Radionuclide therapy has gained increasing importance for the treatment of metastatic, castration-

resistant PC (mCRPC) with the approval of the use of [223]Ra. Systemic administration of the calcium ion mimetic [223]Ra improves survival in mCRPC patients with symptomatic bone metastases [2]. However, about one-third of mCRPC patients present with lymph node or visceral metastases, which are generally associated with a poor prognosis, and are unresponsive to bone-seeking radiopharmaceuticals [3]. Ligands for the prostate-specific membrane antigen (PSMA) have recently been developed to target systemic disease. PSMA is overexpressed in almost all prostate tumours, and is therefore an outstanding target for radionuclide therapy, especially since its expression increases further in patients with dedifferentiated, metastatic or hormone-refractory disease [4]. Several trials have shown effective reductions in tumour burden and serum prostate-specific antigen levels after administration of therapeutically radiolabelled PSMA targeting drugs [5–7].

Based upon promising initial results, a concerted effort has led to the design of PSMA ligands with improved safety profiles. Of several new candidates, ^{177}Lu-labelled DKFZ-PSMA-617 binds with 2.3 nM to PSMA in vitro, and has enhanced binding to tumour in vivo, with relatively reduced uptake in the kidney, an organ at particular risk of treatment-induced toxicity [8]. Before finding general use in the clinic, the dosimetry of ^{177}Lu-DKFZ-PSMA-617 must be defined, so as to enable administration of the optimal treatment activity, allowing tumour irradiation with the maximum absorbed dose without exceeding the recommended thresholds for critical organs. The mode of decay of the radionuclide ^{177}Lu presents a particular advantage for therapeutic dosimetry, as its beta emission provides tumour radiation, while its gamma component allows uptake quantification by serial scintigraphy and SPECT. The aim of this study was to perform image-based absorbed dose calculations for critical organs during two cycles of ^{177}Lu-DKFZ-PSMA-617 administration in a group of mCRPC patients, thus aiding the design of an optimal treatment protocol with minimal toxicity for nontarget organs.

Material and methods

Image acquisition

All data were acquired on a dual-headed Symbia T2 SPECT/CT system (Siemens Medical Solutions, Erlangen, Germany) equipped with medium-energy low-penetration (MELP) collimators and opposing (180° mode) detector heads. Image data were recorded in whole-body planar scintigraphy and SPECT or SPECT/CT mode, i.e. with a SPECT recording followed by a CT acquisition (130 kVp with voxels of size 1 mm×1 mm×5 mm) for SPECT attenuation correction and assessment of patient anatomy. The acquisition parameters are given in Table 1. Energy windows were chosen as described by Delker et al. [9]: the emission window was centred at

Table 1 Acquisition parameters

Parameter	Value
Planar whole-body acquisition	
Matrix	1024×256
Pixel size (mm)	2.4×2.4
Total scan time (min)	20
SPECT acquisition	
Matrix	128×128
Pixel size (mm)	4.8×4.8
Number of steps	128 total (64 per head)
Step duration (s)	20 (40 for calibration)
Approximate total scan time (min)	22

208 keV (width 15 %, the main upper photopeak of the ^{177}Lu decay series), the upper scatter window at 240 keV (width 10 %) and the lower scatter window at 170 keV (width 15 %).

Image reconstruction

Images were reconstructed using a rotation-based one-step-late penalized ordered subsets expectation maximization algorithm which included a gaussian diffusion model to compensate for distance-dependent detector blur [10–13]. The distance-dependent point spread function was derived from measurements of a ^{177}Lu point source positioned at different distances from the detector surface. No corrections for dead time, partial volume and spillover effects were performed. A scatter estimate was derived from the adjacent scatter energy windows with the triple-energy window method, and implemented into the reconstruction algorithm [14]. For attenuation correction, the CT image was segmented based on the method described by Bai et al. [15] by assigning an appropriate Hounsfield unit to each tissue density value, with further conversion to a gamma energy-dependent mass attenuation coefficient, μ. For this purpose we defined our attenuation CT measurements using a tissue characterization phantom (Gammex 467; Gammex, Inc., Middleton, WI). The final image reconstruction is described by Eq. 1,

$$x_j^{k+1} = x_j^k \frac{1}{\sum_{i \in S_n} a_{ij} + \beta\left(P\left(x_j^k\right)\right)} \sum_{i \in S_n} a_{ij} \frac{y_i}{\left(\sum_j a_{ij} x_j^k\right) + s_i} \quad (1)$$

where $P(x_j^k)$ denotes a quadratic filter operation onto voxel j using its 5×5×5 neighbouring voxels, and S_n is the subset of projections to be considered. A penalty weight factor β was of low magnitude in order to slightly reduce the Gibbs artefacts without greatly sacrificing resolution. According to Eq. 1, the final image x^k after iteration k contained the number of reconstructed counts per voxel. Quantitative emission images, obtained as activity concentration per unit volume (i.e. q in

Becquerels per millilitre) in each voxel j, were then calculated as the product of the duration of each tomographic step T (seconds), the voxel volume V (millilitres), and the calibration factor C Becquerels per counts per second):

$$q_j = \frac{x_j}{T \cdot V} \cdot C \qquad (2)$$

Calibration

The calibration factor C in Eq. 2 was derived from a cylindrical phantom with a volume of 6.7 L and an internal diameter of 22 cm, which was homogeneously filled with a solution containing a total ^{177}Lu activity of 637 MBq (Q=92.3 kBq/mL). A SPECT acquisition was performed with 40 s per step, followed by CT imaging, as described above. As can be seen from Eq. 2, the calibration factor does not change with varying step length of the SPECT projections. To avoid a noise-related bias of this factor we decided to achieve an increased number of counts by prolonging the calibration measurements compared to the patient acquisitions. After image reconstruction, C was calculated using Eq. 2, knowing q=Q, T=40 s and V= 0.48 cm^3.

Quantification of recovery

The reproducibility of quantitative values was assessed using a hot-sphere phantom (NEMA-NM2-2001) containing six spheres of internal diameters (and corresponding volumes) of 37 mm (26.5 mL), 28 mm (11.5 mL), 22 mm (5.6 mL), 17 mm (2.6 mL), 13 mm (1.2 mL) and 10 mm (0.5 mL) in a homogeneously filled background volume. A ^{177}Lu activity of 38.1 MBq was added to a measuring cylinder containing 50.8 mL water (75.6 kBq/mL); this solution was used to fill the spheres. A ^{177}Lu activity of 725.4 MBq was mixed in the 9.7-L background volume (7.5 kBq/mL), resulting in a hot sphere to background radioactivity concentration ratio of approximately 10:1. The NEMA phantom was then scanned using the parameters given in Table 1, followed by a CT acquisition. After reconstruction and calibration, the images were further analysed using PMOD software (v.3.603; PMOD Technologies Ltd.). A large cylindrical background volume of interest (VOI) was positioned in the homogeneously filled lower area of the phantom, at least 3 cm from the boundaries. A VOI for each hot sphere was precisely drawn onto the contours of the coregistered CT image. From the mean reconstructed activity concentration q in each VOI, and knowing its true activity concentration, Q, the corresponding recovery coefficients, R, were calculated as $q/Q \times 100$ %for the background and for each sphere.

Patients and therapy

Between September 2014 and April 2015 five patients with mCRPC refractory to standard therapy (mean age 68 years, range 54 to 81 years) each received two cycles of radioligand therapy (RLT) with ^{177}Lu-DKFZ-PSMA-617 administered at a mean activity of 3.6 GBq (range 3.4 to 3.9 GBq) per cycle. An interval of 10 weeks between the cycles was chosen to allow assessment of subacute toxicity at 4 to 8 weeks after RLT [16]. All patients demonstrated PSMA-avid lesions on pretherapeutic ^{68}Ga-HBED-PSMA PET/CT. Each treatment was performed during a 4-day stay in the Nuclear Medicine Ward, in accordance with German radiation protection laws. Patients received 50 mg prednisolone and 1 L of 0.9 % NaCl intravenously daily until discharge. In order to reduce blood flow and tracer uptake in the parotic and submandibular glands, ice packs were applied locally for 6 h after each RLT. Patients were monitored each day as inpatients, with physical examination and routine blood tests for electrolytes, haematology, liver and kidney function. Patients had serial follow-up examinations including routine blood test at intervals of 2 to 4 weeks after RLT.

For each SPECT scan, patients were positioned supine and feet-first on the camera table. The radiopharmaceutical was infused intravenously in 30 mL saline at a flow rate of 100 mL/h. Blood samples were collected from the contralateral side every 10 min until the start of the first whole-body scintigraphy scan at 1 h after the start of infusion, and once on each subsequent measurement day. Approximately 1 h after the start of the infusion, a whole-body planar scintigraphy scan was acquired and calibrated with the settings described by Delker et al. [9], followed by a SPECT/CT scan of the abdomen. Further planar whole-body and abdominal SPECT measurements were acquired on subsequent days at approximately 24, 48 and 72 h after injection. The acquisition parameters are given in Table 1. The dead time reported by the camera was approximately 8 % on day 0 and approximately 3 % on day 1. Because the CT acquisition was performed only on the therapy day, for attenuation correction, the uncorrected SPECT images for each subsequent emission recording were individually coregistered to the single CT scan using the rigid matching function in the PMOD Fusion Tool with manual correction if deemed necessary. The final reconstruction of quantitative SPECT images was performed using corrections for photon scatter, photon attenuation and distance-dependent detector blur, followed by voxelwise application of the calibration factor presented above. Dosimetry was performed as part of the clinical routine. All patients gave written consent to undergo RLT with subsequent dose evaluation. Dose estimations presented in this study were acquired retrospectively from anonymized patient data. The retrospective study protocol was approved by the local ethics committee, and written informed consent for entry into the study was waived.

Absorbed dose calculations

To calculate the total radioactivity in the kidneys, liver, spleen and selected tumour lesions, time–activity curves, obtained from a VOI analysis of the four serial quantitative SPECT images modelled as described by Delker et al. [9], with a linear interpolation of activity between the start of infusion ($t_0 = 0$) and the time (t_1) of the first SPECT/CT measurement, a linear interpolation between t_1 and the time of the SPECT scan at approximately 24 h (t_2), followed by a monoexponential nonlinear least squares fit to the last three data points using MATLAB (R2011a; The MathWorks, Inc., Natick, MA):

$$q(t) = \begin{cases} \alpha_1 t & 0 \leq t < t_1 \\ \alpha_2 t + q(t_1) & t_1 \leq t < t_2 \\ \alpha_3 e^{\gamma t} & t \geq t_2 \end{cases} \qquad (3)$$

To estimate the absorbed dose, this model time–activity curve was time-integrated and multiplied by the organ specific S value [17], considering only the self-dose fraction. Furthermore, S values were corrected for individual organ mass [18, 19]. For approximating the absorbed dose to the salivary glands, the calibrated planar whole-body images were used, with sphere S values.

Absorbed bone marrow dose estimates were calculated from the sequences of planar whole-body images according to the EANM guidelines [20], including the contributions from the bone marrow self-dose, and cross irradiation from the major source organs and the remainder of the body. The bone marrow self-dose was calculated from the activity concentration of the collected venous blood samples and the red marrow-to-blood activity concentration ratio derived from the patients haematocrit by the method of Sgouros [21]. The cross irradiation from the organs and the remainder of the body was calculated by the method of Traino et al. [22] for more than two source organs, using a linear mass scaling for the cross irradiation from the source organs and a ^{177}Lu-dependent nonlinear mass scaling factor for the red marrow and total body.

Results

Image quantification

The analysis of the calibration phantom yielded a calibration factor of C of 110,058 Bq/cps. The reconstructed SPECT image of the NEMA phantom superimposed on the corresponding CT image is shown in Fig. 1a. The calculated recovery coefficients are shown in Fig. 1b, and summarized in Table 2.

Dosimetry

The following sections summarize the results of dosimetric calculations which performed using planar and SPECT image data and the modelled blood curve measured over 72 h. The planar whole-body images from a representative patient (patient 1, first cycle, in Table 3) are shown in Fig. 2. High uptake was observed in the intestines after approximately 24 h. In the planar images of eight out of ten RLT cycles this late intestinal uptake overlapped with 50 – 70 % of the kidney region. From the series of planar whole-body images, the estimated absorbed dose to the salivary glands was 5.1±1.8 Gy (1.4 Gy/GBq). The serial quantitative SPECT and SPECT/CT images from the same patient, superimposed on the CT data from day 0, are shown in Fig. 3.

In 3D SPECT/CT images tracer accumulation was clearly seen in the liver, spleen and kidneys, notably in the renal cortex. From these images the mean absorbed doses per cycle were determined as 2.2±0.6 Gy (0.6 Gy/GBq) to the kidneys, 0.4±0.2 Gy (0.1 Gy/GBq) to the liver and 0.4 Gy±0.1 Gy (0.1 Gy/GBq) to the spleen. The organ masses underlying these absorbed dose estimates were kidneys 156±47 g (range 94 – 236 g), liver 1,265±393 g (range 925 – 1,904 g), spleen 124±40 g (range 66 – 171 g) and salivary glands 38±5 g (range 31 – 43 g). Uptake in excess of background was also seen for multiple tumour lesions, with progressive accumulation up to 24 h after injection (Fig. 4a). In tumours the mean (± SD) absorbed doses were 19.4±13.5 Gy (5.3±3.7 Gy/GBq, range 5.6 – 46.0 Gy) in 21 representative bone lesions from the five patients, 15.1±19.2 Gy (4.2±5.3 Gy/GBq, range 1.2 – 47.5 Gy) in seven lymph metastases from three of the patients, and 7.5±2.7 Gy (2.1±0.8 Gy/GBq, range 5.9 – 11.5 Gy) in four soft tissue metastases seen in one patient. The maximum observed absorbed dose in tumours was 47.5 Gy (13.1 Gy/GBq). The mean (± SD) calculated tumour-to-kidney ratios were 9.8±7.9 (maximum 33.7) for bone metastases, 6.0±5.8 (maximum 15.2) for lymph node metastases, and 3.7±1.1 (maximum 5.6) for soft tissue metastases.

The absorbed dose to the bone marrow was calculated using a combination of organ cross irradiation calculated from SPECT images, the total unassigned body measurement derived from planar images, and the activity measured in blood samples (Fig. 4b) [20]. The mean (± SD) bone marrow absorbed dose in the five patients was 44.0±18.8 mGy (12.1±5.2 mGy/GBq, range 26.9 – 90.5 mGy) per cycle. Figure 4 shows the time–activity curves in a representative patient. The absorbed dose estimates for the investigated critical organs of each individual patient are presented in Table 3.

Correlation

The relationship between absorbed organ dose estimates calculated for each patient from the first treatment cycle and the
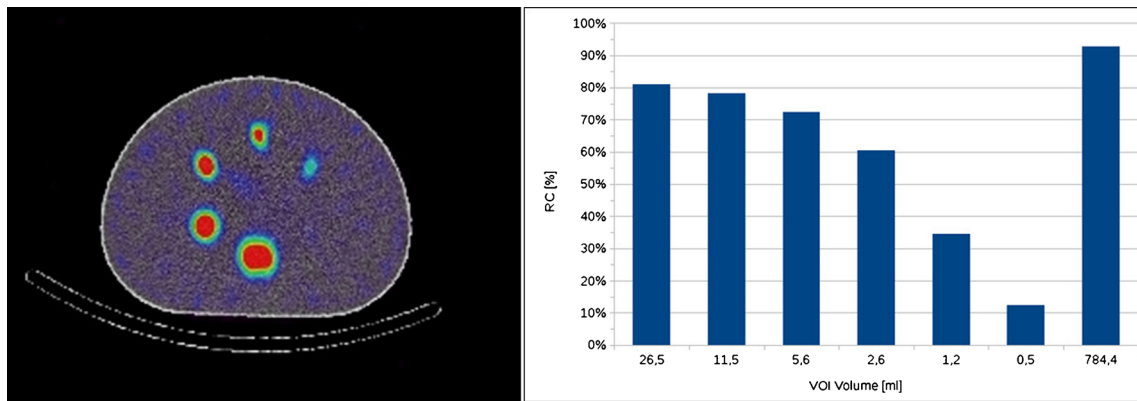
Fig. 1 Fusion of CT and SPECT images of the NEMA phantom (**a**), and the recovery coefficients (*RC*) in percent for each sphere and the 784 mL background (**b**)

corresponding second cycle absorbed doses are shown in Fig. 5. There was a very strong correlation between the absorbed doses of the two cycles, with an overall Pearson's rho of 0.97. In particular, organs with the highest absorbed dose had correlation coefficients of 0.89 (salivary glands) and 0.87 (kidneys). The mean absorbed dose ratios for the kidneys were 0.61 Gy/GBq in cycle 1 and 0.60 Gy/GBq in cycle 2, and for the salivary glands, the mean absorbed dose ratio was 1.41 Gy/GBq for both cycles.

Discussion

The tumour and healthy organ absorbed doses for ^{177}Lu-DKFZ-PSMA-617 were accurately estimated using quantitative SPECT imaging, therefore establishing an optimal treatment protocol for this new RLT. Several advanced image reconstruction procedures are necessary to obtain the activity-corrected quantitative images [23]. We first measured the recovery coefficients of our SPECT images based

on measurements of a known ^{177}Lu activity concentration in a spherical phantom study, from which we derived the best possible reconstruction parameters before proceeding to patient studies. The resultant recovery coefficients of approximately 80 % for spheres of volume greater than 10 mL (Table 2) are in good agreement with the findings of a recent study by Sanders et al. of ^{177}Lu SPECT quantification [24]. The lower recovery coefficients found for the smaller spheres (Fig. 1) most likely arose from the inherently limited spatial resolution, with signals uncorrected for partial volume and spill-over effects. For patient data evaluation, the measurements on day 0 were not included in the fitting to the monoexponential model function since superposition of multiple kinetic phases of the pharmaceutical can occur at these early time points [9]. Hence the influence of errors in these data points, for example the error from the dead time reported by the SPECT system. was reduced and only affected the integral of the linear interpolations. Although the measurement on day 1 was included in the fit to the model, the effect of the contained dead time error on the total estimated absorbed dose could be expected to be of minor magnitude. However, if the administered activity were substantially increased this issue would require reconsideration.

By applying this image formation process to the measurements obtained after ^{177}Lu-DKFZ-PSMA-617 RLT SPECT/CT serial quantitative fusion images were obtained, as shown in a representative patient in Fig. 3. In accordance with the findings from diagnostic ^{68}Ga-HBED-PSMA PET/CT [25], physiological tracer uptake was seen in the abdominal organs, especially the kidneys. The tracer uptake in tumour lesions increased from day 0 to day 1 after RLT, in contrast to uptake in the abdominal organs, which peaked on the day of treatment, and declined thereafter (Fig. 4a), except in the intestines in which uptake peaked at 48 h. This temporal spatial pattern indicates specific binding of the ^{177}Lu-DKFZ-PSMA-617 to PC metastases.

Table 2 Nominal (*Q*) and reconstructed (*q*) activity concentrations and corresponding recovery coefficients for each sphere and the background

Sphere diameter (mm)	Volume (mL)	Activity concentrations (kBq/mL)		Recovery coefficient (%)
		Nominal (*Q*)	Reconstructed (*q*)	
37	26.5	75.6	62.0	81
28	11.5	75.6	59.8	78
22	5.6	75.6	55.4	72
17	2.6	75.6	46.2	60
13	1.2	75.6	26.3	34
10	0.5	75.6	9.5	12
Background	784.4	7.5	7.0	93

Table 3 Administered activity and absorbed dose values for critical organs in each patient during the first and second cycles of RLT

Patient no.	Cycle	Activity (GBq)	Dose					
			Left kidney (Gy/GBq)	Right kidney (Gy/GBq)	Liver (Gy/GBq)	Spleen (Gy/GBq)	Salivary glands (Gy/GBq)	Bone marrow (mGy/GBq)
1	First	3.4	0.57	0.58	0.13	0.11	1.60	7.92
1	Second	3.5	0.54	0.74	0.12	0.10	1.36	9.45
2	First	3.8	0.35	0.38	0.06	0.05	1.38	7.68
2	Second	3.7	0.27	0.33	0.06	0.07	1.12	9.23
3	First	3.6	0.73	0.69	0.12	0.12	1.18	25.13
3	Second	3.9	0.71	0.63	0.11	0.10	1.19	9.36
4	First	3.7	0.52	0.57	0.12	0.13	2.11	12.21
4	Second	3.5	0.61	0.57	0.25	0.17	2.48	10.77
5	First	3.6	0.91	0.81	0.09	0.09	0.76	15.81
5	Second	3.6	0.75	0.81	0.06	0.10	0.91	13.79
	Mean	3.6	0.60	0.61	0.11	0.10	1.41	12.14
	SD	0.1	0.19	0.16	0.06	0.03	0.53	5.24

In the planar scintigraphy whole-body images, somewhat elevated ^{177}Lu-DKFZ-PSMA-617 accumulation was observed in the salivary glands and to a lesser extent in the mucosa. The ^{177}Lu-signal in the intestine (Fig. 2) overlapped significantly with the kidneys, as has also been reported by others [25–28], in most of the planar images after RLT. This overlap would probably result in overestimation of the absorbed kidney dose if the calculation of dosimetry relied on planar images, or hybrid SPECT and planar acquisitions. We therefore recommend that quantitative SPECT acquisition be used to estimate absorbed kidney doses in ^{177}Lu-DKFZ-PSMA-617 RLT.

We calculated mean absorbed doses of 0.6 Gy/GBq for the kidneys, 0.1 Gy/GBq for the liver, 0.1 Gy/GBq for the spleen and 1.4 Gy/GBq for the salivary glands. The high physiological uptake in healthy salivary glands was also noted by

Fig. 2 Anterior planar whole-body images at (**a**) 1, (**b**) 24, (**c**) 48, and (**d**) 72 h in a representative patient (Table 3, patient 1, first cycle)
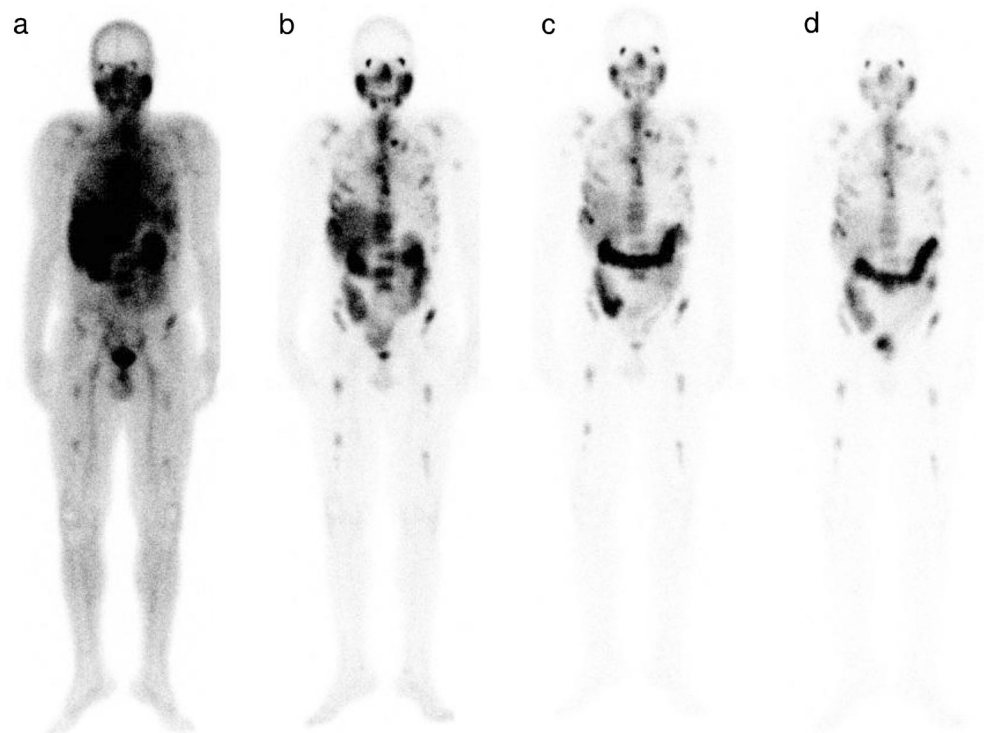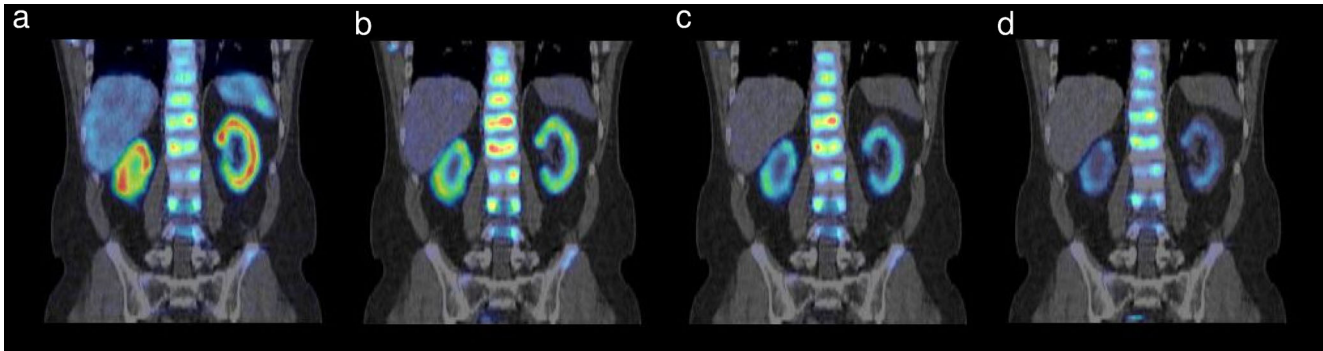
Fig. 3 Serial fused SPECT/CT coronal images at (**a**) 1, (**b**) 24, (**c**) 48, and (**d**) 72 h in the same patient as in Fig. 2

Zechmann et al. [5], who performed dosimetric estimations with ^{131}I-labelled PSMA compounds. Although the estimated maximum cumulative absorbed dose after two cycles was up to 16 Gy (patient 4) to the salivary glands, none of our patients complained of xerostomia during follow-up. This is also in accordance with findings following external beam radiation therapy, with which irreversible damage to the salivary glands was observed in only a small group of patients after administration of less than 30 – 40 Gy [29, 30]. We found a lower absorbed dose to the liver following ^{177}Lu-DKFZ-PSMA-617 RLT than was reported for ^{131}I-MIP-1095 [5], and indeed a lower absorbed dose to all of the evaluated organs than was seen with the ^{177}Lu-labelled PSMA antibody J-591 [31, 32], indicating a superior safety profile for ^{177}Lu-DKFZ-PSMA-617 RLT.

Bone marrow is known to be a tissue at critical risk in targeted radionuclide therapy [21, 33–35]. In our study, the absorbed bone marrow dose (0.012 Gy/GBq per cycle), as estimated from blood and imaging data, was substantially below the critical level of 2 Gy [33], even when taking into account multiple therapy cycles. This predicts that bone marrow toxicity is unlikely to be encountered with ^{177}Lu-DKFZ-PSMA-617 RLT at the expected activity ranges of several gigabecquerels per cycle. Nevertheless high radioactivity accumulations in bone metastases, which lie close to or within

the red marrow, indicate that the true absorbed dose to some domains of active marrow may be somewhat higher than estimated in our study due to spillover.

The kidneys, because of their vital function in elimination of xenobiotics, are the dose limiting organ in a number of radioreceptor therapies [36, 37], as in the present study, in which the dose to the kidneys was the highest amongst the evaluated abdominal organs. The mean absorbed dose to the kidneys which was determined in this study for ^{177}Lu-DKFZ-PSMA-617 is comparable to the dose to the kidneys for ^{177}Lu-DOTATATE previously reported by Sandström et al. [38] in a large number of patients (0.6 Gy/GBq) . Moreover, ^{177}Lu-DKFZ-PSMA-617 showed higher tumour-to-kidney uptake for all investigated metastases (median 5.8) than ^{177}Lu-DOTA-JR11 (median 3.3) or ^{177}Lu-DOTATATE (median 1.6) in a previous study by Wild et al. [39]. Our results further suggest that the kidney absorbed dose is comfortably below commonly- applied dose constraints for that organ (e.g. 23 Gy as reported by Emami et al. [40]). We therefore conclude that the amount of ^{177}Lu-DKFZ-PSMA-617 activity administered in each cycle can safely be increased to achieve an even higher absorbed tumour dose without causing damage to the kidneys. The maximum absorbed kidney dose in two cycles was 6.0 Gy (patient 5, Table 3), which is just one-quarter of the maximal absorbed dose cited above. Based on these results,
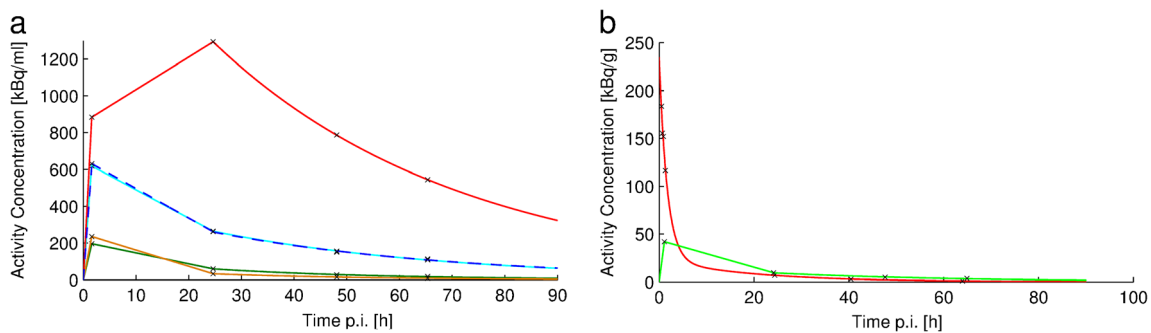
Fig. 4 **a** Dose model curves of activity concentrations in a representative patient (Table 3, patient 1, first cycle) in one tumour metastasis (*red*), kidneys (*cyan and dashed blue*), spleen (*orange*) and liver (*green*). **b** Activity concentration curves from the blood samples (*red*) and the whole body (*green*) for calculation of the bone marrow dose
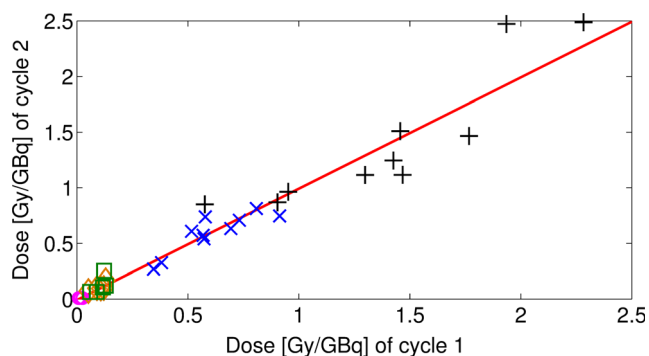
Fig. 5 Correlation between organ doses from first therapy cycle (abscissa) and the second therapy cycle (ordinate) including the salivary glands (*black pluses*), the kidneys (*blue crosses*), the liver (*green squares*), the spleen (*orange diamonds*) and the bone marrow (*purple circles*). The red line is the linear regression line. The individual tissue doses between the two therapy cycles were strongly correlated with Pearson's rho of 0.97

we predict that it would be safe to increase the administered activity of the first cycle to, for example, 6 GBq in analogy to the recommendations of Bodei et al. for peptide receptor radionuclide therapy in neuroendocrine tumours [41], and adapt the activity for the following cycles based on the dosimetry to optimize the tumour dose without reaching the limiting organ dose. Even in our patient with the highest radiation burden, this would yield an absorbed kidney dose for the first cycle of only 5 Gy, well below the safety limit.

Although none of our patients complained of any effects on salivary gland function after therapy, it is a matter of concern that increasing the activity might put the salivary glands at risk. Compared to the radioactive iodine-labelled compounds such as ^{131}I-MIP-1095 [5], the novel radiopharmaceutical ^{177}Lu-DKFZ-PSMA-617 has favourable characteristics, imparting lower absorbed doses to critical organs, including the bone marrow, which predicts less-severe side effects. Furthermore, the chelation of ^{177}Lu-based pharmaceuticals can be carried out more quickly and easily compared with ^{131}I-based labelling, and the physical properties of ^{177}Lu compared with those of ^{131}I may allow shorter inpatient stays, improve the quality of dosimetric image data and reduce therapy-related toxicity. In this study the estimated absorbed doses (notably for the critical organs) were highly correlated between the two therapy cycles, as also observed by Garske et al. [42]. Exceptions are the estimated bone marrow doses in the two therapy cycles in patient 3 (25.13 mGy/GBq and 9.36 mGy/GBq) and the absorbed liver doses in patient 4 (0.12 Gy/GBq and 0.25 Gy/GBq). The calculated absorbed doses for the other organs in these two patients were consistent between the therapy cycles. Because of the good correlation in all patients we conclude that the absorbed dose

of the following therapy cycle can be predicted with sufficient accuracy. This could allow adaptation of the activity to be administered in the following therapy cycle.

Conclusion and outlook

Our absorbed dose estimate results derived from five mCRPC patients each undergoing two cycles of RLT with ^{177}Lu-DKFZ-PSMA-617 are encouraging. The highest absorbed dose to healthy organs was observed in the salivary glands, but this was not associated with any symptoms of xerostomia during the observation period. The highest accumulated absorbed kidney dose after both therapy cycles was one-quarter of the critical dose for that organ. Based on these findings, we suggest a more aggressive treatment, starting with an activity of 6.0 GBq and modulating the activity for the following cycles based on dosimetry to reach a preset threshold which is assumed save. For optimized dosimetry we recommend using quantitative SPECT.

References

1. Lozano R, Naghavi M, Foreman K, Lim S, Shibuya K, Aboyans V, et al. Global and regional mortality from 235 causes of death for 20 age groups in 1990 and 2010: a systematic analysis for the Global Burden of Disease Study 2010. Lancet. 2012;380:2095–128.
2. Parker C, Nilsson S, Heinrich D, Helle SI, O'Sullivan JM, Fossa SD, et al. Alpha emitter radium-223 and survival in metastatic prostate cancer. N Engl J Med. 2013;369:213–23.
3. Pond GR, Sonpavde G, de Wit R, Eisenberger MA, Tannock IF, Armstrong AJ. The prognostic importance of metastatic site in men with metastatic castration-resistant prostate cancer. Eur Urol. 2014;65:3–6.
4. Ghosh A, Heston WD. Tumor target prostate specific membrane antigen (PSMA) and its regulation in prostate cancer. J Cell Biochem. 2004;91:528–39.
5. Zechmann CM, Afshar-Oromieh A, Armor T, Stubbs JB, Mier W, Hadaschik B, et al. Radiation dosimetry and first therapy results with a (124)I/(131)I-labeled small molecule (MIP-1095) targeting

PSMA for prostate cancer therapy. Eur J Nucl Med Mol Imaging. 2014;41:1280–92.

6. Tagawa ST, Milowsky MI, Morris M, Vallabhajosula S, Christos P, Akhtar NH, et al. Phase II study of lutetium-177-labeled anti-prostate-specific membrane antigen monoclonal antibody J591 for metastatic castration-resistant prostate cancer. Clin Cancer Res. 2013;19:5182–91.

7. Milowsky MI, Nanus DM, Kostakoglu L, Vallabhajosula S, Goldsmith SJ, Bander NH. Phase I trial of yttrium-90-labeled anti-prostate-specific membrane antigen monoclonal antibody J591 for androgen-independent prostate cancer. J Clin Oncol. 2004;22: 2522–31.

8. Benesova M, Schafer M, Bauder-Wust U, Afshar-Oromieh A, Kratochwil C, Mier W, et al. Preclinical evaluation of a tailor-made DOTA-conjugated PSMA inhibitor with optimized linker moiety for imaging and endoradiotherapy of prostate cancer. J Nucl Med. 2015;56:914–20.

9. Delker A, Ilhan H, Zach C, Brosch J, Gildehaus F-J, Lehner S, et al. The influence of early measurements onto the estimated kidney dose in 177Lu-DOTATATE peptide receptor radiotherapy of neuroendocrine tumors. Mol Imaging Biol. 2015. doi:10.1007/s11307-015-0839-3.

10. Kohli V, King MA, Glick SJ, Pan TS. Comparison of frequency-distance relationship and gaussian-diffusion-based methods of compensation for distance-dependent spatial resolution in SPECT imaging. Phys Med Biol. 1998;43:1025–37.

11. Hudson HM, Larkin RS. Accelerated image reconstruction using ordered subsets of projection data. IEEE Trans Med Imaging. 1994;13:601–9.

12. Wallis JW, Miller TR. An optimal rotator for iterative reconstruction. IEEE Trans Med Imaging. 1997;16:118–23.

13. Green PJ. Bayesian reconstructions from emission tomography data using a modified EM algorithm. IEEE Trans Med Imaging. 1990;9: 84–93.

14. Beekman FJ, Kamphuis C, Frey EC. Scatter compensation methods in 3D iterative SPECT reconstruction: a simulation study. Phys Med Biol. 1997;42:1619–32.

15. Bai CY, Shao L, Da Silva AJ, Zhao Z. A generalized model for the conversion from CT numbers to linear attenuation coefficients. IEEE Trans Nucl Sci. 2003;50:1510–5.

16. Kwekkeboom DJ, de Herder WW, Kam BL, van Eijck CH, van Essen M, Kooij PP, et al. Treatment with the radiolabeled somatostatin analog [177Lu-DOTA0, Tyr3] octreotate: toxicity, efficacy, and survival. J Clin Oncol. 2008;26:2124–30.

17. Stabin MS, Hunt, J, Brill, A, Sparks R, Eckerman K, Bertelli L. RADAR: the radiation dose assessment resource. www.doseinfo-radar.com. 2001.

18. Stabin MG, Siegel JA. Physical models and dose factors for use in internal dose assessment. Health Phys. 2003;85:294–310.

19. Williams LE, Liu A, Yamauchi DM, Lopatin G, Raubitschek AA, Wong JY. The two types of correction of absorbed dose estimates for internal emitters. Cancer. 2002;94:1231–4.

20. Hindorf C, Glatting G, Chiesa C, Linden O, Flux G; EANM Dosimetry Committee. EANM Dosimetry Committee guidelines for bone marrow and whole-body dosimetry. Eur J Nucl Med Mol Imaging. 2010;37:1238–50.

21. Sgouros G. Bone marrow dosimetry for radioimmunotherapy: theoretical considerations. J Nucl Med. 1993;34:689–94.

22. Traino AC, Ferrari M, Cremonesi M, Stabin MG. Influence of total-body mass on the scaling of S-factors for patient-specific, blood-based red-marrow dosimetry. Phys Med Biol. 2007;52:5231–48.

23. Dewaraja YK, Frey EC, Sgouros G, Brill AB, Roberson P, Zanzonico PB, et al. MIRD pamphlet No. 23: quantitative SPECT for patient-specific 3-dimensional dosimetry in internal radionuclide therapy. J Nucl Med. 2012;53:1310–25.

24. Sanders J, Kuwert T, Hornegger J, Ritt P. Quantitative SPECT/CT imaging of 177Lu with in vivo validation in patients undergoing peptide receptor radionuclide therapy. Mol Imaging Biol. 2015;17: 585–93.

25. Afshar-Oromieh A, Malcher A, Eder M, Eisenhut M, Linhart H, Hadaschik B, et al. PET imaging with a [68Ga]gallium-labelled PSMA ligand for the diagnosis of prostate cancer: biodistribution in humans and first evaluation of tumour lesions. Eur J Nucl Med Mol Imaging. 2013;40:486–95.

26. Gordon IO, Tretiakova MS, Noffsinger AE, Hart J, Reuter VE, Al-Ahmadie HA. Prostate-specific membrane antigen expression in regeneration and repair. Mod Pathol. 2008;21:1421–7.

27. Maraj B, Aldersley M, Markham A. Prostate-specific membrane antigen expression in the duodenum: implications in coeliac disease and immunotherapy for prostate cancer. Lancet. 1998;351:1559–60.

28. Silver DA, Pellicer I, Fair WR, Heston W, Cordon-Cardo C. Prostate-specific membrane antigen expression in normal and malignant human tissues. Clin Cancer Res. 1997;3:81–5.

29. Gensheimer MF, Liao JJ, Garden AS, Laramore GE, Parvathaneni U. Submandibular gland-sparing radiation therapy for locally advanced oropharyngeal squamous cell carcinoma: patterns of failure and xerostomia outcomes. Radiat Oncol. 2014;9:255.

30. Hey J, Setz J, Gerlach R, Janich M, Hildebrandt G, Vordermark D, et al. Parotid gland-recovery after radiotherapy in the head and neck region – 36 months follow-up of a prospective clinical study. Radiat Oncol. 2011;6:125.

31. Bander NH, Milowsky MI, Nanus DM, Kostakoglu L, Vallabhajosula S, Goldsmith SJ. Phase I trial of 177lutetium-labeled J591, a monoclonal antibody to prostate-specific membrane antigen, in patients with androgen-independent prostate cancer. J Clin Oncol. 2005;23:4591–601.

32. Vallabhajosula S, Kuji I, Hamacher KA, Konishi S, Kostakoglu L, Kothari PA, et al. Pharmacokinetics and biodistribution of 111In-and 177Lu-labeled J591 antibody specific for prostate-specific membrane antigen: prediction of 90Y-J591 radiation dosimetry based on 111In or 177Lu? J Nucl Med. 2005;46:634–41.

33. Forrer F, Krenning EP, Kooij PP, Bernard BF, Konijnenberg M, Bakker WH, et al. Bone marrow dosimetry in peptide receptor radionuclide therapy with [177Lu-DOTA0, Tyr3] octreotate. Eur J Nucl Med Mol Imaging. 2009;36:1138–46.

34. Larson SM, Raubitschek A, Reynolds JC, Neumann RD, Hellstrom K-E, Hellstrom I, et al. Comparison of bone marrow dosimetry and toxic effect of high dose 131I-labeled monoclonal antibodies administered to man. Int J Radiat Appl Instrumen B. 1989;16:153–8.

35. Siegel J, Wessels B, Watson E, Stabin M, Vriesendorp H, Bradley E, et al. Bone marrow dosimetry and toxicity for radioimmunotherapy. Antibody Immunoconjug Radiopharm. 1990;3:213–34.

36. Bodei L, Cremonesi M, Grana CM, Chinol M, Baio SM, Severi S, et al. Yttrium-labelled peptides for therapy of NET. Eur J Nucl Med Mol Imaging. 2012;39:93–102.

37. Kam B, Teunissen J, Krenning E, De Herder W, Khan S, van Vliet E, et al. Lutetium-labelled peptides for therapy of neuroendocrine tumours. Eur J Nucl Med Mol Imaging. 2012;39:103–12.

38. Sandström M, Garske-Román U, Granberg D, Johansson S, Widström C, Eriksson B, et al. Individualized dosimetry of kidney and bone marrow in patients undergoing 177Lu-DOTA-octreotate treatment. J Nucl Med. 2013;54:33–41.

39. Wild D, Fani M, Fischer R, Del Pozzo L, Kaul F, Krebs S, et al. Comparison of somatostatin receptor agonist and antagonist for peptide receptor radionuclide therapy: a pilot study. J Nucl Med. 2014;55:1248–52.

40. Emami B, Lyman J, Brown A, Cola L, Goitein M, Munzenrider J, et al. Tolerance of normal tissue to therapeutic irradiation. Int J Radiat Oncol Biol Phys. 1991;21:109–22.

41. Bodei L, Mueller-Brand J, Baum RP, Pavel ME, Horsch D, O'Dorisio MS, et al. The joint IAEA, EANM, and SNMMI practical guidance on peptide receptor radionuclide therapy (PRRNT)

in neuroendocrine tumours. Eur J Nucl Med Mol Imaging. 2013;40:800–16.

42. Garske U, Sandström M, Johansson S, Sundin A, Granberg D, Eriksson B, et al. Minor changes in effective half-life during fractionated 177Lu-octreotate therapy. Acta Oncol. 2012;51:86–96.

List of Figures

Danksagung